JOURNAL OF GEOPHYSICAL RESEARCH, VOL. 113, D16S44, doi:10.1029/2007JD008814, 2008



# Global observations of $HNO_3$ from the High Resolution Dynamics Limb Sounder (HIRDLS): First results

D. E. Kinnison,[1] J. Gille,[1,2] J. Barnett,[3] C. Randall,[2,4] V. L. Harvey,[4] A. Lambert,[5] R. Khosravi,[1] M. J. Alexander,[6] P. F. Bernath,[7,8] C. D. Boone,[7] C. Cavanaugh,[1] M. Coffey,[1] C. Craig,[1] V. C. Dean,[2] T. Eden,[1] D. Ellis,[2] D. W. Fahey,[9] G. Francis,[1] C. Halvorson,[1] J. Hannigan,[1] C. Hartsough,[1] C. Hepplewhite,[3] C. Krinsky,[2] H. Lee,[1,10] B. Mankin,[1] T. P. Marcy,[9,11] S. Massie,[1] B. Nardi,[1] D. Packman,[1] P. J. Popp,[9,11] M. L. Santee,[5] V. Yudin,[1] and K. A. Walker[7,12]

Received 15 April 2007; revised 5 November 2007; accepted 21 February 2008; published 3 July 2008.

[1] We present the first evaluation of the $HNO_3$ data product (version 2.04.09) from the High Resolution Dynamics Limb Sounder (HIRDLS) on the Earth Observing System (EOS) Aura satellite. The HIRDLS instrument obtains between 5000 and 7000 $HNO_3$ profiles per day. HIRDLS $HNO_3$ data are generally good over the latitude range of 64°S to 80°N and pressure range 100 to 10 hPa, with some profiles, depending on latitude, having useful information between 100 to 161 hPa. The individual profile ''measured'' precision is between 10 and 15%, but can be much larger if the $HNO_3$ abundance is low or outside the 100 hPa to 10 hPa range. Global results are compared with the $HNO_3$ observations from version 2.2 of the EOS Aura Microwave Limb Sounder (MLS), and it is found that large-scale features are consistent between the two instruments. HIRDLS $HNO_3$ is biased 0–20% low relative to Aura MLS in the mid-to-high latitudes and biased high in the tropical stratosphere. HIRDLS $HNO_3$ is also compared with Atmospheric Chemistry Experiment Fourier Transform Spectrometer (ACE-FTS). In these mostly high-latitude comparisons the HIRDLS $HNO_3$ data are biased 10–30% low, depending on altitude. Finally, the HIRDLS $HNO_3$ is compared to in situ data taken by the NOAA Chemical Ionization Mass Spectrometer (CIMS) instrument flown during the 2005 NASA Houston Aura Validation Experiment (AVE) and the ability of HIRDLS to measure $HNO_3$ in the UTLS region is examined.

**Citation:** Kinnison, D. E., et al. (2008), Global observations of $HNO_3$ from the High Resolution Dynamics Limb Sounder (HIRDLS): First results, *J. Geophys. Res.*, *113*, D16S44, doi:10.1029/2007JD008814.

## 1. Introduction

[2] The EOS Aura satellite was launched on 15 July 2004 into a 705 km sun-synchronous near polar orbit. EOS Aura carries four instruments: the Ozone Monitoring Instrument (OMI), the Tropospheric Emission Spectrometer (TES), the Microwave Limb Sounder (MLS), and the High Resolution Dynamics Limb Sounder (HIRDLS). The Aura instruments were designed to measure tropospheric and stratospheric ozone, short-lived trace gases that affect ozone abundance, along with many long-lived tracers [*Schoeberl et al.*, 2006]. This paper describes the first validation results of one constituent, nitric acid ($HNO_3$), from the HIRDLS instrument.

[3] $HNO_3$ is formed by a gas-phase three-body reaction of $NO_2$ with the hydroxyl radical (OH) and a third molecule [*Austin et al.*, 1986]. It is destroyed by gas-phase reaction with OH and by photolysis. The lifetime of $HNO_3$ varies from approximately one month in the lower stratosphere to one hour in the upper stratosphere [*Brasseur and Solomon*, 2005]. $HNO_3$ is also formed by heterogeneous reactions on

[1]National Center for Atmospheric Research, Boulder, Colorado, USA.
[2]University of Colorado, Boulder, Colorado, USA.
[3]Atmospheric, Oceanic and Planetary Physics Department, Oxford University, Oxford, UK.
[4]Laboratory for Atmospheric and Space Physics, Boulder, Colorado, USA.
[5]Jet Propulsion Laboratory, Pasadena, California, USA.
[6]NorthWest Research Associates, Boulder, Colorado, USA.
[7]Department of Chemistry, University of Waterloo, Waterloo, Ontario, Canada.
[8]Department of Chemistry, University of York, York, UK.
[9]Chemical Science Division, Boulder, Earth System Research Laboratory, National Oceanic and Atmospheric Administration, Boulder, Colorado, USA.
[10]Deceased 6 July 2007.
[11]Also at Cooperative Institute for Research in Environmental Sciences, University of Colorado, Boulder, Colorado, USA.
[12]Department of Physics, University of Toronto, Toronto, Ontario, Canada.


0148-0227/08/2007JD008814$09.00

background sulfate aerosol [*Hofmann and Solomon*, 1989] and polar stratospheric clouds (PSCs) [*Solomon et al.*, 1986; *Solomon*, 1999]. In fact, one form of solid PSCs is nitric acid tri-hydrate (NAT) [*Toon et al.*, 1986; *Crutzen and Arnold*, 1986; *Voigt et al.*, 2000; *Höpfner et al.*, 2006]. NAT is believed to contribute to denitrification of the polar lower stratosphere [see *Fahey et al.*, 2001, and reference therein]. Liquid PSC particles also affect the local distribution of $HNO_3$. Observations [*Dye et al.*, 1992; *Arnold*, 1992] and theoretical studies [*Carslaw et al.*, 1994; *Tabazadeh et al.*, 1994] have demonstrated that some PSCs are composed of liquid supercooled ternary solutions (STS) of $HNO_3$-$H_2SO_4$-$H_2O$. Unlike solid nitric acid hydrate PSCs, these liquid PSCs show a continuous increase in particle volume with decreasing temperature. The uptake of gas-phase $HNO_3$ into STS aerosol will locally "denoxify" the atmosphere; however, the mean diameter of these aerosols is relatively small (<1 $\mu$m) and the particle settling is not considered important; therefore, little denitrification will occur.

[4] $HNO_3$ is an important minor constituent in the stratosphere because it is the main reservoir species in the $NO_X$ family, whose active members (NO, $NO_2$) take part in one of the major catalytic cycles for stratospheric ozone loss [*Crutzen*, 1971; *Johnston*, 1971]. Insofar as formation of $HNO_3$ reduces the abundance of NO and $NO_2$, it also impacts the importance of gas-phase $NO_X$ chemistry in ozone loss. In addition, $HNO_3$ formed on stratospheric clouds can act to denitrify the polar lower stratosphere, as noted above, and thus enable the activation of chlorine species that cause the formation of the springtime "ozone hole."

[5] The first global observations of $HNO_3$ were based on the Limb Infrared Monitor of Stratospheric (LIMS) launched on the Nimbus 7 spacecraft [*Gille et al.*, 1980; *Gille and Russell*, 1984; *Gille et al.*, 1984]. These measurements were based on a limb scanning six-channel infrared (IR) radiometer. The LIMS mission had a lifetime of seven months (25 October 1978 through 28 May 1979) and derived $HNO_3$ abundances in a latitude region from 64°S to 84°N, from 100 hPa to 2 hPa. Results from this mission produced the first global $HNO_3$ reference climatology [see *Gille et al.*, 1987, 1993].

[6] In 1991, two $HNO_3$ observing instruments were launched on the Upper Atmosphere Research Satellite (UARS): the Cryogenic Limb Array Etalon Spectrometer (CLAES) instrument [*Roche et al.*, 1994] and the Microwave Limb Sounder (MLS) [*Waters et al.*, 1999; *Santee et al.*, 1995, 1997, 1998]. $HNO_3$ data from the UARS CLAES instrument was added to the LIMS $HNO_3$ reference climatology of *Gille et al.* [1998]. Multiple studies were performed using the UARS MLS $HNO_3$ observations to examine the role of $HNO_3$ in polar ozone depletion [e.g., *Santee et al.*, 1995, 1997, 1998, 2000, 2002]. A three-dimensional $HNO_3$ climatology from the UARS MLS observations was published by *Santee et al.* [2004].

[7] Additional global measurements of $HNO_3$ have been obtained from the Improved Limb Atmospheric Spectrometer (ILAS), which was launched on board the Advanced Earth Observing Satellite (ADEOS) in August 1996. $HNO_3$ observations are available between November 1996 and June 1997. This instrument is a solar occultation satellite sensor, which measures $HNO_3$ in the IR region of the solar spectrum [*Koike et al.*, 2000; *Pan et al.*, 2002]. A follow-on ILAS instrument, ILAS-II, launched on ADEOS-II, also observed global distributions of $HNO_3$ [*Irie et al.*, 2006]. $HNO_3$ observations by ILAS-II are available between April and October 2003. Global $HNO_3$ observations are also available on the Odin satellite from the Sub-millimeter Radiometer (SMR) instrument [*Urban et al.*, 2005]. This instrument was launched on 20 February 2001 and is still in operation. The Michelson Interferometer for Passive Atmospheric Sounding (MIPAS) aboard the Environmental Satellite (ENVISAT) also measures stratospheric $HNO_3$ [*Mengistu Tsidu et al.*, 2005; *Wang et al.*, 2007]. Two additional global $HNO_3$ observing instruments have recently been launched. The first is the Atmospheric Chemistry Experiment Fourier Transform Spectrometer (ACE-FTS) [*Bernath et al.*, 2005] and the second is a follow-on version of the UARS MLS instrument that was also launched on the EOS Aura satellite [*Waters et al.*, 2006; *Santee et al.*, 2005, 2007]. Results from both of these instruments will be shown below and compared to HIRDLS observations.

[8] The remainder of the paper is divided up into four sections: section 2 gives an overview of the HIRDLS instrument, comparing its pre- and post-launch capabilities; section 3 presents a discussion of the HIRDLS $HNO_3$ vertical resolution and precision; section 4 compares HIRDLS $HNO_3$ to Aura MLS and ACE-FTS measurement; section 5 examines HIRDLS observations of $HNO_3$ in the UTLS region; and section 6 gives a summary and conclusions.

## 2. HIRDLS Instrument Overview

[9] This section is divided into two parts. The first summarizes the prelaunch HIRDLS instrument capabilities to measure $HNO_3$ and the second describes the impact on these capabilities of the partial blockage of the instrument aperture that occurred during launch.

### 2.1. Prelaunch HIRDLS

[10] The HIRDLS instrument is a limb scanning 21-channel IR filter radiometer. The limb scanning measurement technique is based on previous work and is described by *Gille and House* [1971], *Gille and Russell* [1984], and *Taylor et al.* [1993]. The prelaunch HIRDLS instrument is described by *Gille and Barnett* [1992, 1996] and *Edwards et al.* [1995]. The HIRDLS experiment is designed to measure temperature, ten trace gases ($O_3$, $HNO_3$, $H_2O$, $N_2O$, $CH_4$, CFC-11, CFC-12, $ClONO_2$, $NO_2$, and $N_2O_5$), as well as cloud top heights and aerosol extinction profiles.

[11] The primary channel for retrieval of HIRDLS $HNO_3$ is channel 8, having a band pass of 840–928 $cm^{-1}$ [*Edwards et al.*, 1995; T. Eden et al., Spectral characterization of the HIRDLS flight instrument from pre-launch calibration data, manuscript in preparation, 2008]. However, because the spectra of CFC-11 (channel 7) and CFC-12 (channel 9) overlap with the spectrum of $HNO_3$, these channels cannot be regarded as independent and the three gases are retrieved simultaneously using channels 7, 8, and 9. The initial guess, a priori, and contaminants are obtained from the NCAR 3-D chemical transport model, MOZART-3

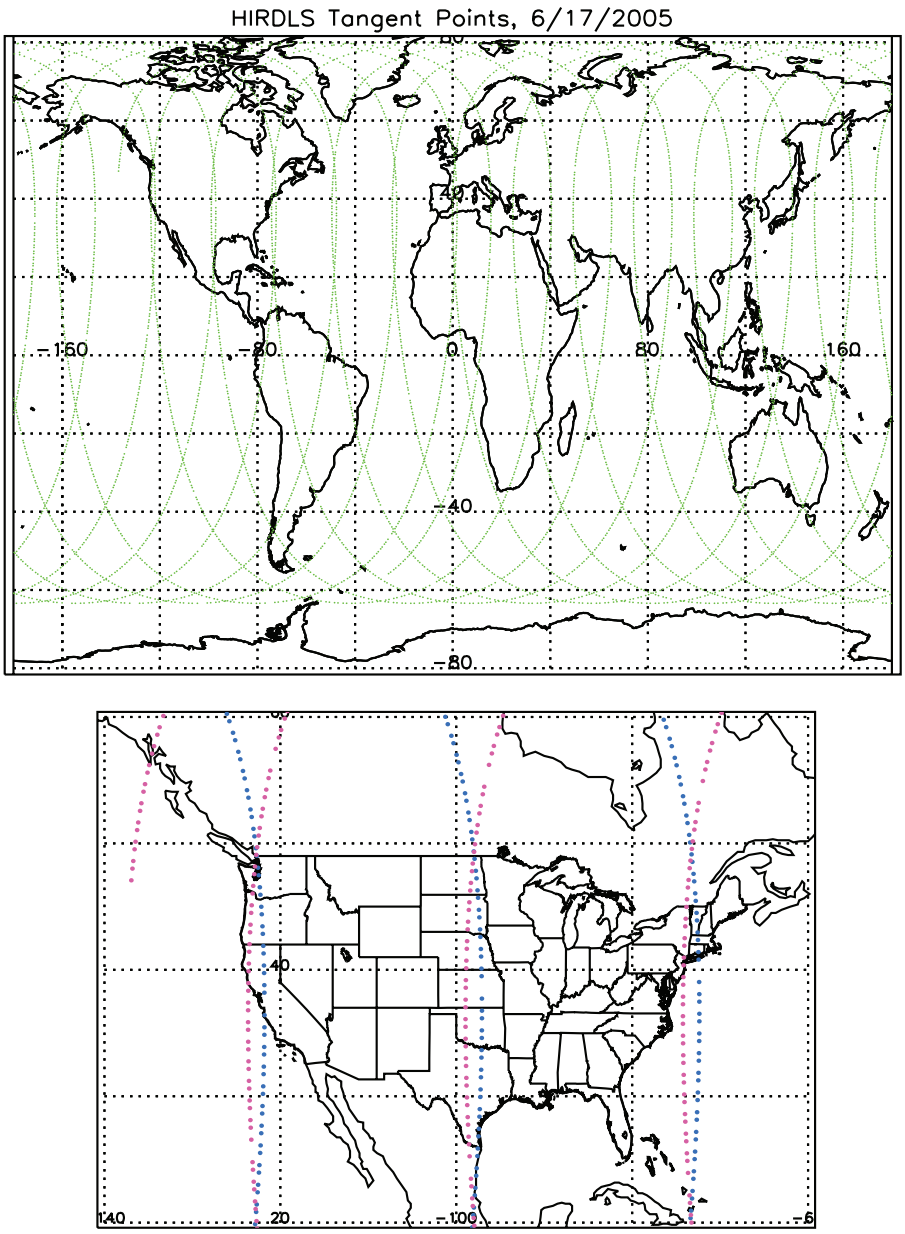


**Figure 1.** Latitude-longitude cross sections showing HIRDLS profile tangent point measurement locations. (top) Green circles show the locations of 1 day of observations (5600 profiles) on 17 June 2005. (bottom) An expanded view of the HIRDLS tangent point profile locations. The ascending (magenta) and descending (blue) orbits are highlighted.

(Model of OZone And Related chemical Tracers, version 3) [*Kinnison et al.*, 2007]. HIRDLS currently incorporates spectroscopic data from HITRANS 2004 [*Rothman et al.*, 2003].

[12] The vertical resolution for $HNO_3$ and most of the remaining retrieved species was designed to be approximately 1 km. The prelaunch horizontal resolution was also designed to be programmable, that is, the azimuth observing position was not fixed to the orbital plane of the spacecraft, but could scan at a given rate and angle. In the prelaunch global observing mode, this would give approximately 7800 profiles per day with pole-pole coverage, with observational tangent points (as measured in the limb) separated by 5° in longitude and 4° in latitude.

### 2.2. Postlaunch HIRDLS

[13] During launch most of the optical aperture was blocked by a torn piece of the instrument's insulation material. Fortunately, this blockage did not completely obscure limb views of the atmosphere. Shortly after launch, it was found that there were azimuth angles furthest from the orbital plane, on the side away from the sun where a partial view of the atmosphere is possible. The postlaunch HIRDLS is essentially fixed at one of these azimuth angles [*Gille et al.*, 2005, 2008]. This fixed azimuth position has the effect of reducing the latitudinal coverage and longitudinal resolution. The tangent point locations for a typical postlaunch day are shown in Figure 1 (top). The postlaunch HIRDLS instrument now covers the latitude range of 64°S

to 80°N and measures 5400–6200 profiles per day with profile spacing at the equator of 24.72° in longitude. The latitudinal resolution is approximately 1° along the orbit track. Figure 1 (bottom) expands the geographic view and highlights the horizontal distance of the coincident ascending and descending orbits.

[14] The blockage of the viewing aperture has not only reduced the incoming atmospheric radiance signal, but has added an addition radiance oscillation as the scan mirror operates in the elevation axis (earth-space direction). During postlaunch several configurations were examined to minimize this oscillation by adjusting the elevation scan rate. These different configurations are defined by operational scan tables [*Gille et al.*, 2008]. Results from two scan tables are shown in this study: scan table 13 (ST13; 28 April 2005 to 24 April 2006); and scan table 23 (ST23; 4 May 2006 to present). These two scan tables include the bulk of HIRDLS $HNO_3$ observations. Scan table 30 (ST30; 21 January 2005 to 28 April 2005) is not discussed in this paper and data derived from this scan table should be used with caution for scientific studies. There is one additional scan table period that is not examined in this paper. This scan table, ST22 (24 April 2006 to 4 May 2006), is nearly identical to ST23 and results shown for ST23 should be considered applicable for ST22. Corrections to the incoming radiance signal are discussed in detail by *Gille et al.* [2005, 2008]. Fortunately, the incoming atmospheric radiance signal for the $HNO_3$ channel is relatively large and the HIRDLS level-2 processor is capable of retrieving $HNO_3$ even with the above mentioned interferences present.

[15] The HIRDLS level-2 retrieval algorithm is described in detail by *Lambert et al.* [1999]. The algorithm is based on optimal estimation theory, using a maximum a posteriori solution method [*Rodgers*, 2000]. The objective of this approach is to obtain vertical profiles of atmospheric constituents for which the algorithm's radiative transfer model generates radiances that are consistent with those measured. The solution is constrained by a priori knowledge of the atmospheric state and the measurement uncertainties.

[16] The results described in this paper use HIRDLS data version 2.04.09. We do not examine the entire HIRDLS measurement period, but only select days-of-interest (DOI). These DOI have primarily been chosen according to the availability of correlative data.

## 3. Vertical Resolution and Precision

[17] This section examines the HIRDLS $HNO_3$ vertical resolution as derived from knowledge of the HIRDLS $HNO_3$ averaging kernels. The HIRDLS $HNO_3$ precision is also examined. The precision is shown in two ways. The first approach is derived from the HIRDLS level-2 retrieval algorithm. We label this precision the HIRDLS $HNO_3$ "theoretical" precision. This is a lower estimate of the true precision. The second approach examines measurements during summer seasons where atmospheric variability is minimized. We label this precision the HIRDLS $HNO_3$ "measured" precision.

### 3.1. Vertical Resolution

[18] The vertical resolution for the HIRDLS $HNO_3$ can be described by examining the $HNO_3$ averaging kernels for given regions of the atmosphere [*Rodgers*, 2000]. Examples of the HIRDLS averaging kernels for $HNO_3$ are shown in Figure 2. Figure 2 depicts the averaging kernels for $HNO_3$ on 21 June 2006 at 1.5°N, 45.3°N, and 63°S, denoted by the green lines. The red line is the integrated area under each kernel, where values of unity indicate that the majority of the information for that vertical region is coming from the measurements and not the a priori estimate. The full-width half-maximum (FWHM) of each averaging kernel is an indication of the vertical resolution of the $HNO_3$ measurement. This is shown in Figure 2 (right, blue lines). The $HNO_3$ vertical resolution is approximately 1.1 km in the tropics (Figure 2, top), between 21 and 35 km. In this region most of the information for the retrieval is coming from the measurements. Below 20 km, the a priori estimate contributes to a greater extent; in fact, at 17 km 50% of the retrieved $HNO_3$ is coming from the a priori estimate. At 45°N (Figure 2, middle) and 63°S (Figure 2, bottom) latitudes, the vertical resolution is approximately 1.1 km between 15 and 41 km and 15–36 km respectively. The averaging kernel and vertical resolution figure will be discussed in section 5 when HIRDLS measurements are examined in the UTLS region.

### 3.2. Theoretical Precision

[19] The optimal estimation retrieval algorithm calculates a total retrieval error, which is a combination of the a priori error, and the propagation errors of the radiance measurements [*Lambert et al.*, 1999]. In Figure 3 the fractional error contribution is shown for the same three latitudes as in Figure 2. In this figure the fractional error is divided into the forward model error (blue line), the measurement error (red line), and the a priori error (green line). The forward model error represents the uncertainty of the physics of the measurement including the representation of the instrument and the radiative transfer processes. The HIRDLS forward model and radiative transfer details specific to HIRDLS are described by *Francis et al.* [2006]. The measurement error includes contributions from instrument noise for each channel. It is assumed that the instrument noise is uncorrelated between channels. This component of the HIRDLS fractional error was scaled up to take account for the reduction in the postlaunch atmospheric signal due the instrument blockage. The a priori error represents the uncertainty in the state of the atmosphere and its expected variability. The total retrieval error, commonly called the solution error is constructed assuming Gaussian distributions for the individual components described above. In Figure 3 (top) the equatorial profiles of the individual components of the $HNO_3$ fractional error are shown. Between 22 and 35 km the fractional total retrieval error is <0.3 and the measurement error dominates. Below and above this region the a priori error is the largest contributor to the fractional total retrieval error. In Figure 3 (middle), profiles of fractional errors are shown at 45.3°N. At this latitude there is a higher abundance of $HNO_3$ over a broader vertical range and therefore the fractional total retrieval error is 0.3 or less between 15 and 35 km and the measurement error dominates the total retrieval error above 25 km. Below 25 km down to approximately 16 km the forward model error is the dominant contributor to the total retrieval error. Below 16 km the a priori error is dominant error term. In Figure 3

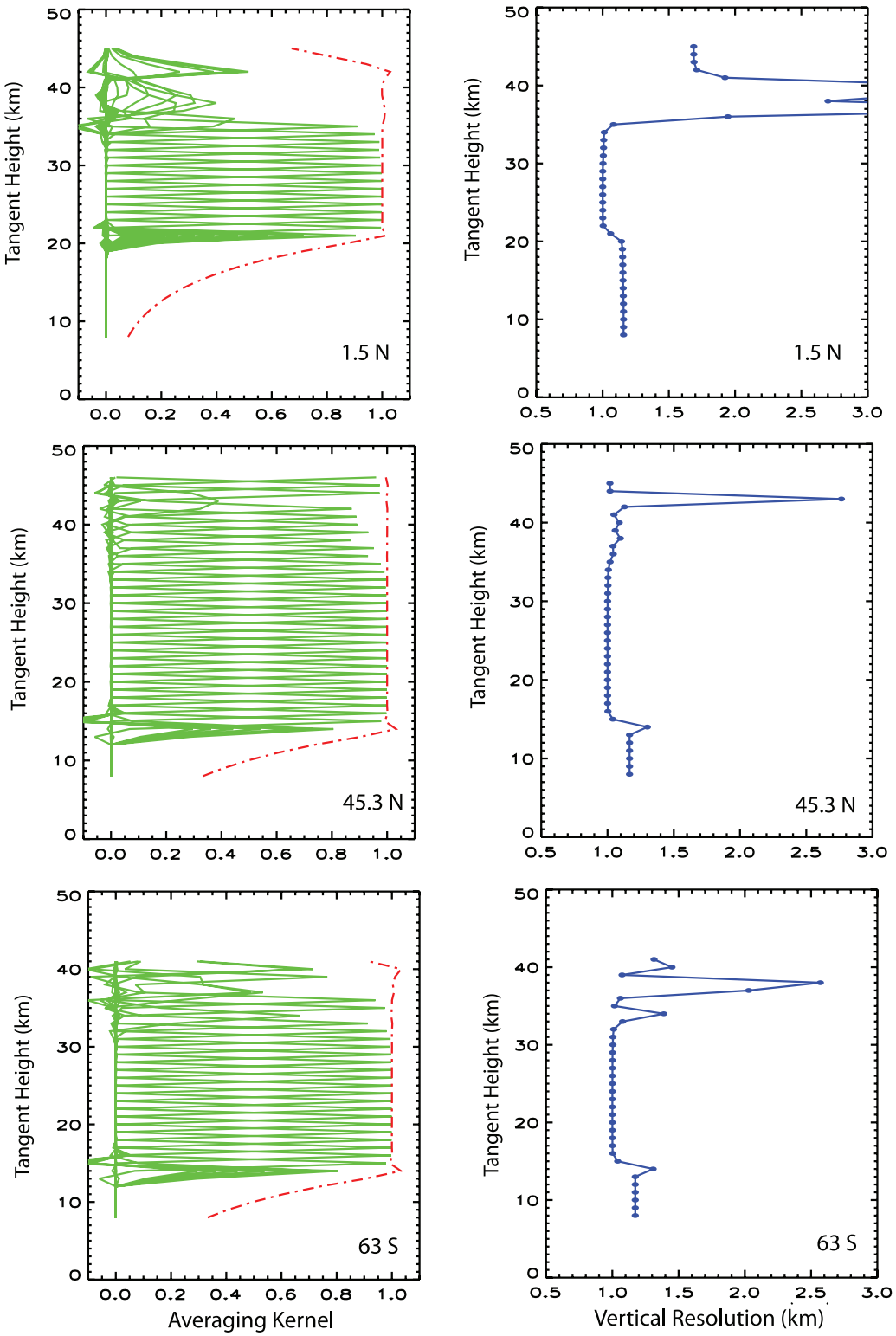


**Figure 2.** HIRDLS $HNO_3$ averaging kernels and full width half maximum (FWHM) vertical resolution profiles are shown on 21 June 2006 at 1.5°N, 45.3°N, and 63°S. (left) Averaging kernels (green lines) and the integrated area under each kernel (red line). (right) Vertical resolution as derived from the FWHM of each kernel (blue line).

(bottom), a Southern Hemisphere high-latitude region is shown. The overall breakdown of the individual components of the total retrieval error is similar to the midlatitude Northern Hemisphere region, except that the vertical extent of the region where the error is <0.3 is slightly smaller (i.e., 15–32 km). This analysis is not meant to be an exhaustive description of all retrieval errors, under all atmospheric conditions, but it does highlight where one should expect

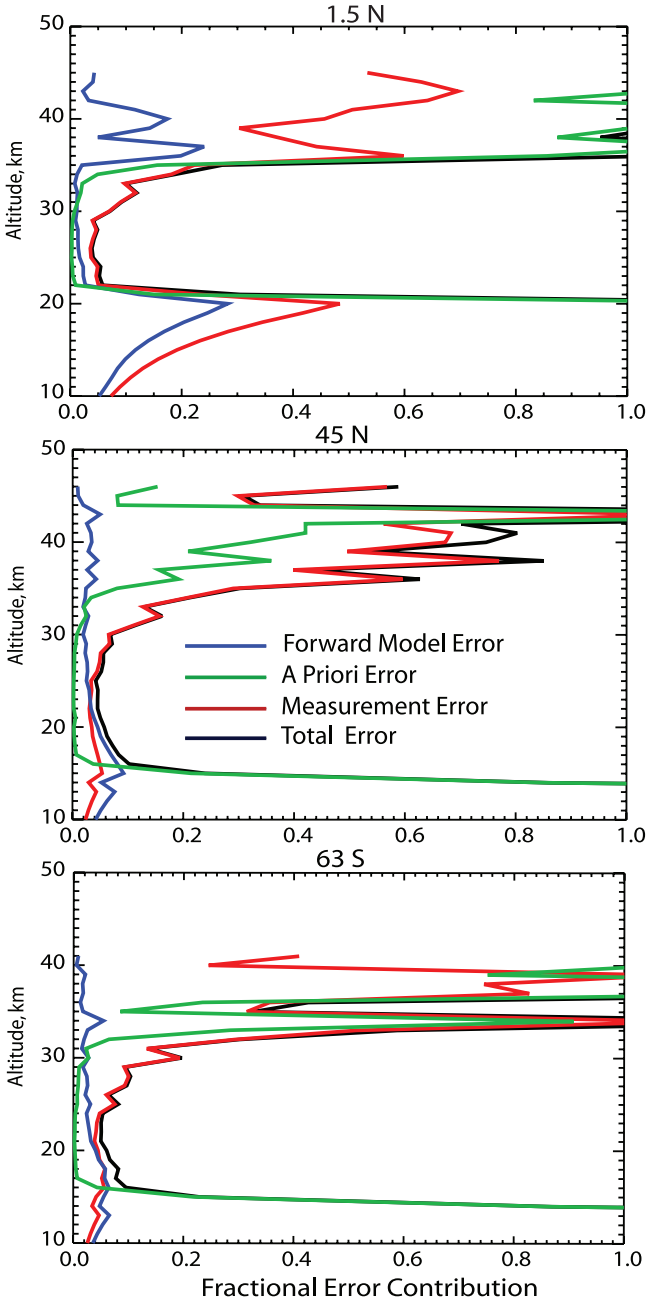


**Figure 3.** HIRDLS $HNO_3$ fractional error contribution for 21 June 2006 for latitudes (top) 1.5°N, (middle) 45.3°N, and (bottom) 63°S. The forward model error (blue line), the a priori error (green line), and the measurement error (red line), along with the total retrieval error (black line) are shown.

HIRDLS observations to be most appropriate for science applications. In the following discussion, the total fractional error or variance will be denoted as the fractional "theoretical precision." This "theoretical precision" is a standard output product of all HIRDLS level-2 retrievals.

[20] In Figure 4, the theoretical precision (in units of percent instead of fractional abundance) is shown for the two main operational scan tables used in the HIRDLS data. Results from scan tables 13 and 23 are shown in Figure 4, top and bottom, respectively. The vertical region between 161 and 100 hPa, 100–10 hPa, and 10–1.9 hPa are shown in Figure 4, left, middle, and right columns, respectively. In the region where the $HNO_3$ abundance is relatively large (100–10 hPa; Figure 4, middle column), approximately 80% of the observed $HNO_3$ has a theoretical precision of $\leq$10%. In Figure 4, left column (161–100 hPa region), 40% of the measurements have a theoretical precision of $\leq$10%. In Figure 4, right column (10–1.9 hPa), scan tables 13 and 23 have only 5% of the theoretical precision in the of $\leq$10% bin. Overall, Figure 4 states that the two scan tables give comparable theoretical precision in the three regions of the atmosphere shown.

[21] For all the validation comparisons shown below, we have filtered the HIRDLS data to use only results that have a level-2 theoretical precision of $\leq$30%. This threshold is somewhat arbitrary, but it does guarantee that the retrieved HIRDLS $HNO_3$ product will have minimal contribution from the a priori estimate, forward model, and measurement errors (see Figure 3).

### 3.3. Observed Standard Deviation (Measured Precision)

[22] Another measure of the precision of the HIRDLS $HNO_3$ observations is the variability within regions of the atmosphere where geophysical variability is at a minimum. In this work we call this estimate of the precision the "measured precision." To examine the observed variability, 24 h of HIRDLS $HNO_3$ were interpolated onto a potential temperature grid and then assembled into 4° equivalent latitude bins centered on 1° increments (essentially 4° wide box-car smoothing in equivalent latitude). The equivalent latitude was derived from Met Office potential vorticity data. In addition, in order to compare air parcels with similar insolation, an additional criterion was imposed. This criterion limits measurements to within 5 degrees of the average geographic latitude in each equivalent latitude bin. Figure 5 shows results for this type of analysis. Figure 5 (top) examines a day in December 2006, and Figure 5 (bottom) examines a day in June 2006. The potential temperature range is from 300 to 1000 K or approximately 10 to 35 km. The minimum observed standard deviation is approximately 10% in Figure 5. This occurs in the summer hemisphere of both plots of Figure 5, where atmospheric variability is known to be a minimum and $HNO_3$ is abundant (typically > 4 ppbv). The theoretical precision (not shown) approaches 5% in this region, as discussed in sections 3.1 and 3.2. Figure 5 supports the derivation of the theoretical precision obtained from the level-2 retrieval. On the basis of this analysis, the theoretical precision may be an underestimate of the true precision, but the error would be on the order of 5% in regions of relatively high abundance of $HNO_3$.

## 4. Comparisons With Correlative Data

[23] This section compares HIRDLS $HNO_3$ with Aura MLS and SCISAT-1 ACE-FTS $HNO_3$ measurements. The HIRDLS/ACE-FTS coincident comparisons are made at mid-to-high latitudes. The HIRDLS/MLS coincident comparisons are for the range of HIRDLS measurements (i.e.,

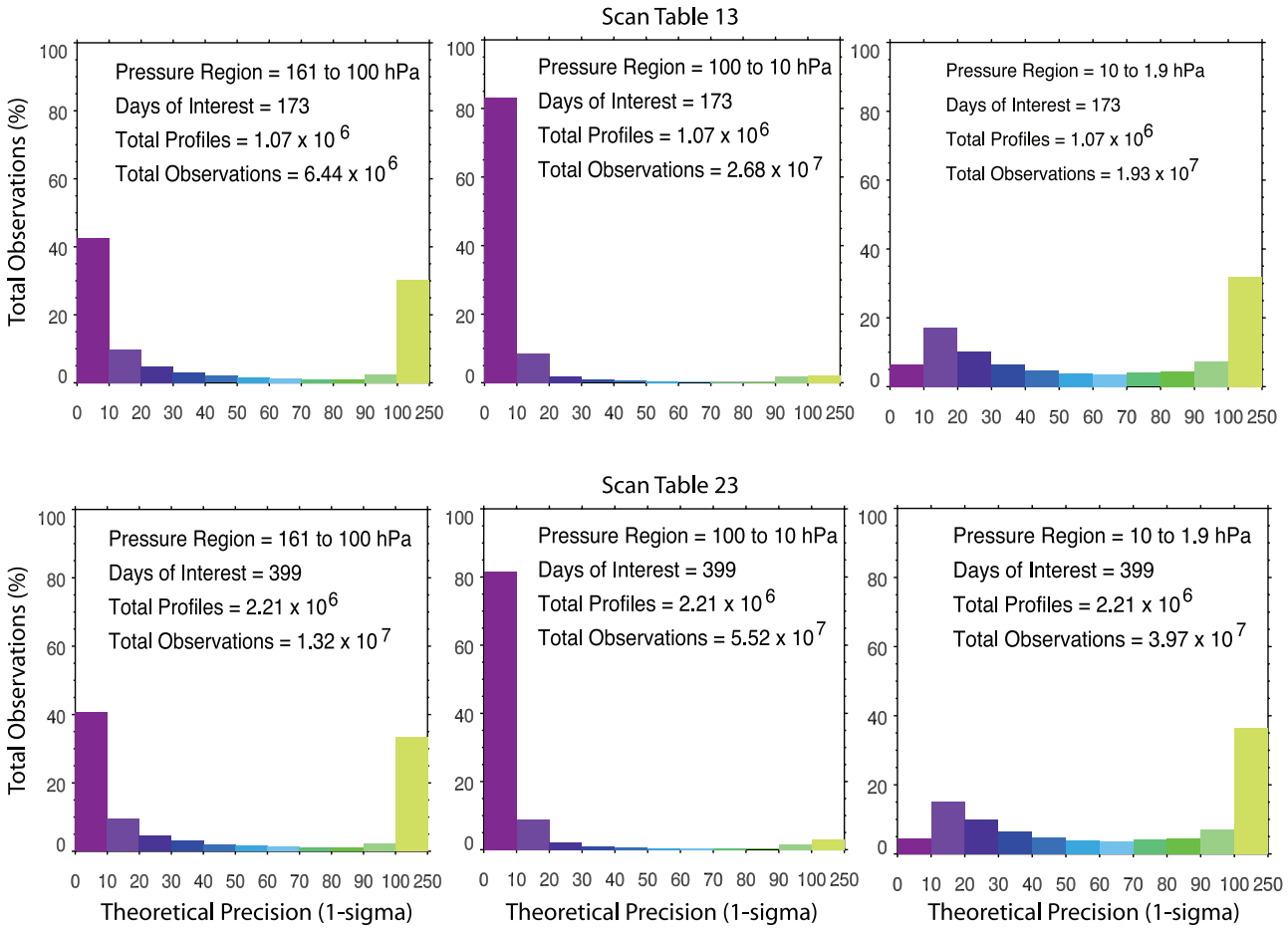


**Figure 4.** Theoretical precision (1-$\sigma$) for the two HIRDLS scan tables as described in the text. The theoretical precision is shown as a percentage of the total observations within a given theoretical precision bin. Scan tables (top) 13 and (bottom) 23 observations in the (left) 161–100 hPa, (middle) 100–10 hPa, and (right) 10–1.9 hPa regions. The total observations included in the analysis are the sum of all the retrieval points included in each pressure region of the HIRDLS $HNO_3$ profile, for each day included in the analysis.

64°S to 80°N). These correlative data sets have been compared to each other by *Santee et al.* [2007].

### 4.1. Aura MLS

[24] In this section we compare the global distribution of HIRDLS $HNO_3$ to Aura MLS $HNO_3$ [*Santee et al.*, 2007]. Current data availability allows comparisons of $HNO_3$ from HIRDLS v2.04.09 and MLS v2.2 to be made on multiple days from launch to the present. We show zonal mean distributions and differences for latitude-height cross sections (average of multiple days of observations), followed by latitude-longitude cross sections for individual days. These types of comparisons show how comparable the global structure of $HNO_3$ is between HIRDLS and MLS. These comparisons are followed by a statistical comparison of coincidence differences using a larger group of DOIs.

[25] In Figure 6, three representative periods are shown. For the results shown in each plot of Figure 6, MLS $HNO_3$ data were linearly interpolated in log pressure to the HIRDLS pressure levels, and both HIRDLS and MLS data were binned every 2.5° latitude and 30° longitude. MLS v2.2 quality and status values were also used to screen MLS data. Latitude-height zonal mean distributions for three periods are shown along with their differences. In the top row, selected days are averaged for May 2006. The $HNO_3$ hemispherical asymmetry (i.e., higher $HNO_3$ abundance in the Southern Hemisphere) is observed in both Aura MLS and HIRDLS observations. This is consistent with our understanding of the seasonal evolution of $HNO_3$ as derived from previous satellite observations (e.g., LIMS observations [*Gille et al.*, 1998]). In the mid- to high-latitude region, in both hemispheres, HIRDLS $HNO_3$ is 0–20% less than Aura MLS (see Figure 6, right). The line of 0% difference for HIRDLS minus MLS is the separation between the white and blue contours. In Figure 6 (middle and bottom), selected days are averaged for October 2006 and March 2007 respectively. The $HNO_3$ hemispherical asymmetry is such that there is a higher abundance of $HNO_3$ in the Northern Hemisphere in both HIRDLS and Aura MLS observations for the October period. There is approximately the same abundance of $HNO_3$ in both hemispheres in the March period. This is also consistent with current under-

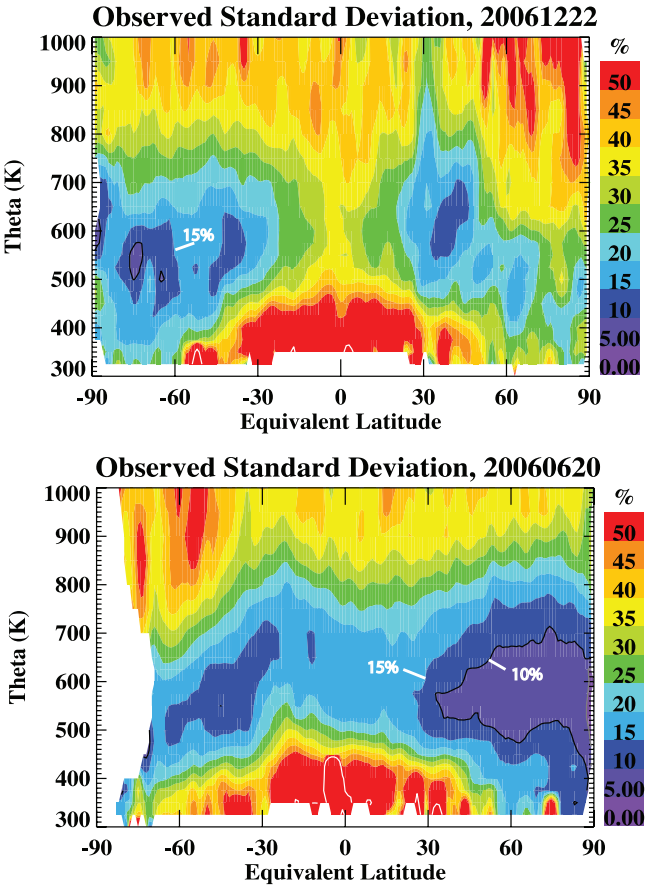


**Figure 5.** $HNO_3$ standard deviation in a potential temperature and equivalent latitude coordinate system. Results are given for 2 days, (top) 22 December 2006 and (bottom) 20 June 2006. Standard deviation units are given in terms of percentage of $HNO_3$ mixing ratio. The black lines highlight the 10% contour.

standing of $HNO_3$ seasonal evolution. The HIRDLS minus MLS percentage difference plots for these periods in the mid-to-high latitudes also show that HIRDLS is 0–20% less than MLS. In the tropics, the differences are much larger, at least for the May (Figure 6, top) and March (Figure 6, bottom) comparisons. In this region, near 30 hPa, HIRDLS $HNO_3$ can be >50% higher than MLS. For Figure 6 (middle), the 30 hPa tropical difference between HIRDLS and MLS are near 0%. When one examines the days that make up these averages, it is found that the variability in the percentage differences comes from the variability in the MLS $HNO_3$ observations. Further analysis is needed to reconcile which data set is correct.

[26] In Figures 7 and 8, $HNO_3$ longitude-latitude cross sections are shown for 28 October 2006 and 3 March 2007, respectively. The top and bottom rows for Figures 7 and 8 are for 51.1 hPa and 31.6 hPa, respectively. The purpose of this comparison is to determine whether HIRDLS $HNO_3$ observations represent the same synoptic-scale features as observed by Aura MLS. From Figures 7 and 8 it is clear that the HIRDLS and Aura MLS instruments detect the same variability in their respective $HNO_3$ retrievals. For example, in Figure 7 (top) in the high-latitudes Northern Hemisphere, there are maximum values of $HNO_3$ abundance in both HIRDLS and Aura MLS between the 90°E longitude and the Greenwich Meridian. In Figure 7 (second row), there is also a consistent maximum in $HNO_3$ between HIRDLS and Aura MLS near the southern tip of South America. Figure 8 also shows common features between the two data sets, for example, there is another consistent maximum in $HNO_3$ abundances over Canada for both pressure surfaces. Overall, the HIRDLS $HNO_3$ horizontal structure is very consistent with Aura MLS.

[27] In Figure 9, coincident differences for HIRDLS minus MLS are shown for scan tables 13 and 23. There are 92 and 42 DOIs used in Figure 9, with approximately 1600 and 1800 coincidences per day, giving a total of 165,513 and 67,595 coincidences for scan tables 13 and 23, respectively. This figure was constructed by dividing the measurements into bins 1° in latitude by 24° in longitude. In each bin, for every HIRDLS $HNO_3$ profile, every MLS $HNO_3$ profile was located that was within a distance of 500 km and 4 h. If there was more than one profile, the closest MLS profile (by distance) was called the coincidence. This was done for each DOI. The coincident differences for each day were then averaged into 10° zonal average bins. For the final overall differences shown in Figure 9, the daily zonal mean coincident differences were averaged and the percentage and absolute magnitudes were plotted. The results from this larger sampling of coincidences is similar to Figure 6; that is, the mid-to-high latitudes differences show that HIRDLS $HNO_3$ is biased low between 0 and 20%. There is also a similar HIRDLS high bias in the tropics near 30 hPa when more DOIs are included. There are also changes in the tropics between 100 hPa and 60 hPa that become quite substantial. This is a region where HIRDLS is not very sensitive to retrieving $HNO_3$ (see Figures 2 and 3). Absolute changes in units of ppbv are also shown for completeness.

### 4.2. ACE-FTS

[28] This section compares HIRDLS $HNO_3$ relative to ACE-FTS observations. NASA launched the ACE-FTS on the Canadian SCISAT-1 satellite on 12 August 2003. The FTS instrument measures IR radiation in the 2.2–12.3 $\mu$m region with a spectral resolution of 0.02 $cm^{-1}$. The ACE-FTS, a solar occultation instrument, with orbit inclination 74°, obtains near global coverage over the course of a year, but the majority of the measurements occur in the polar regions [*Bernath et al.*, 2005; *Walker et al.*, 2005]. Version 2.2 of the ACE-FTS retrievals was used [*Boone et al.*, 2005] and the $HNO_3$ precision is about 3%. Here, $HNO_3$ retrievals employ 'micro windows' in the ranges 867–880 $cm^{-1}$ and 1691–1729 $cm^{-1}$. The altitude range for the version 2.2 $HNO_3$ retrievals is 5 to 37 km, with a vertical resolution of ~4 km. Interfering species included in the retrievals were $O_3$ and $H_2O$. The accuracy is still under investigation, owing to uncertainties in the $HNO_3$ bands used in the ACE-FTS retrievals. However, recent comparisons with MIPAS showed that coincident differences were typically within 10% [*Wang et al.*, 2007].

[29] HIRDLS and ACE-FTS coincidences were defined as occurring within 2 h in time and 500 km. There were a

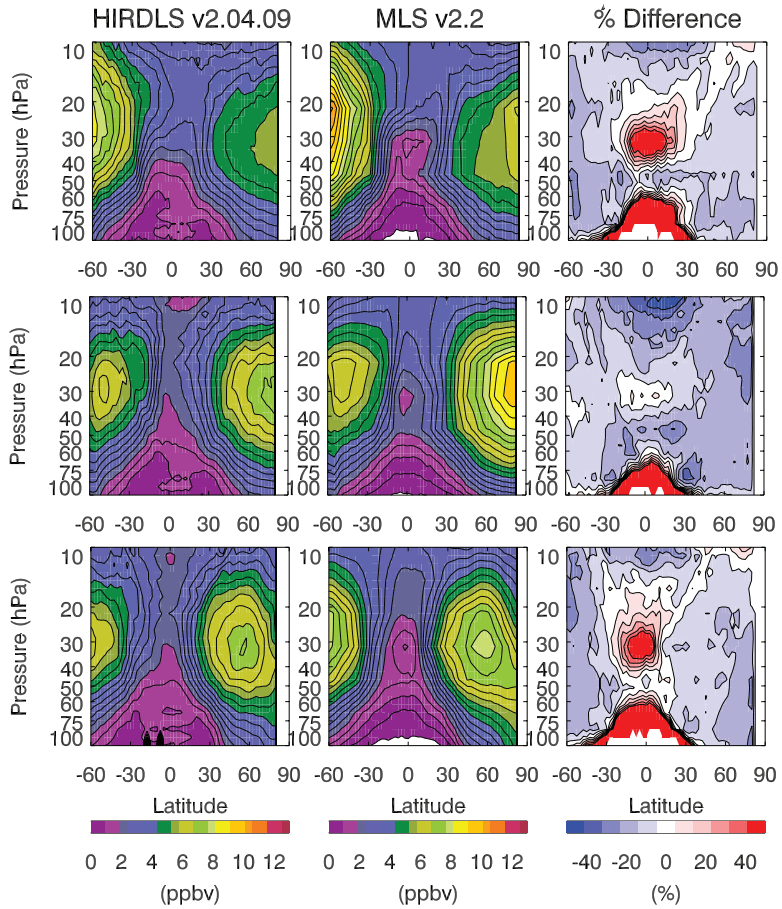


**Figure 6.** Latitude-height cross sections for HIRDLS and MLS $HNO_3$ (ppbv). (top) A zonal mean average of 4 days (in May 2006). (middle) A zonal mean average of 8 days (in October 2006). (bottom) A zonal mean average of 27 days (in March 2007). The percentage difference of (HIRDLS – MLS / MLS) is also shown. The zero percentage difference contour line is the transition from white to blue.

total of 512 HIRDLS/ACE-FTS coincident comparison for scan table 13 taken between 23 May 2005 and 15 April 2006; 389 and 123 of these coincidences were between 42°N and 81°N and 41°S and 67°S, respectively. There were 150 HIRDLS/ACE-FTS coincident comparisons for scan table 23 taken between 19 May 2006 and 28 October 2006; 120 and 30 of these coincidences were between 64°N and 73°N and 40°S and 65°S, respectively. Note that there were often numerous HIRDLS profiles coincident with a single ACE-FTS profile. When this occurred, the coincident HIRDLS profiles are averaged together and the average profile is compared to the ACE-FTS profile. Figure 10 shows the location of each ACE-FTS/HIRDLS coincidence.

[30] Because the coincidences occurred primarily at high latitudes in the Northern and Southern Hemispheres, the two regions have been compared separately. Figure 11 shows the statistical differences between the HIRDLS and ACE-FTS coincidence profiles for the period of scan table 13. The top row is for all the coincident difference profiles in the Northern Hemisphere and the bottom row is for all coincidence profile differences in the Southern Hemisphere. The left column shows absolute differences, while the right column shows percentage differences. These differences were calculated as HIRDLS minus ACE-FTS (relative to ACE-FTS for the % differences). There is a clear low bias in the HIRDLS $HNO_3$ observations relative to ACE-FTS. In the Northern Hemisphere, the mean maximum absolute low bias is 2 ppbv near 40–50 hPa. This corresponds to a mean low bias of 20% in this region. In the Southern Hemisphere, the maximum HIRDLS $HNO_3$ absolute mean low bias is 1.6 ppbv near 40 hPa. This also corresponds to a HIRDLS $HNO_3$ low bias of approximately 20% in this region. In both the Northern and Southern Hemisphere comparisons, the coincident percentage difference change is not constant with altitude. In the Northern Hemisphere, HIRDLS $HNO_3$ is biased low relative to ACE-FTS by 10% and 30% at 10 hPa and 100 hPa respectively. As one goes higher in pressure (lower in altitude), the coincidence percentage difference becomes larger, and HIRDLS $HNO_3$ is bias low by 40% at 200 hPa. In the Southern Hemisphere, HIRDLS $HNO_3$ is consistent with ACE-FTS $HNO_3$ at 10 hPa, but biased low by 30% at 100 hPa and by 40% at 200 hPa.

[31] In Figure 12, the statistical differences between the HIRDLS and ACE-FTS coincidence are shown for the period of scan table 23. In the Northern Hemisphere, near 40 hPa, HIRDLS $HNO_3$ is biased low by 20% relative to ACE-FTS. As was the case in Figure 11, coincident percentage differences are not constant between 10 hPa and

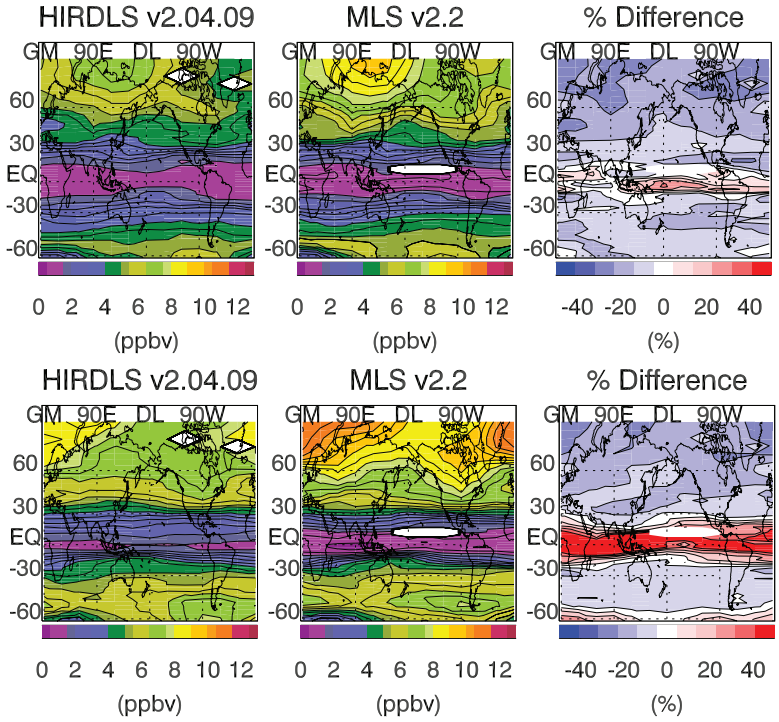


**Figure 7.** Longitude-latitude cross sections of HIRDLS and MLS $HNO_3$ (ppbv) on 28 October 2006 for (top) 51.1 hPa and (bottom) 31.6 hPa. The percentage difference of (HIRDLS – MLS / MLS) is also shown. The zero percentage difference contour line is the transition from white to blue.

100 hPa. HIRDLS $HNO_3$ is consistent with ACE-FTS $HNO_3$ at 10 hPa, but is low by 30% at 100 hPa. This low bias in HIRDLS $HNO_3$ relative to ACE-FTS $HNO_3$ for scan table 23 is similar to the result for scan table 13. HIRDLS $HNO_3$ in the Southern Hemisphere is also biased low relative to ACE-FTS between 100 hPa and 10 hPa. In this hemisphere, the HIRDLS $HNO_3$ are biased low relative to ACT-FTS $HNO_3$ by 20% between 10 hPa and 40 hPa. This

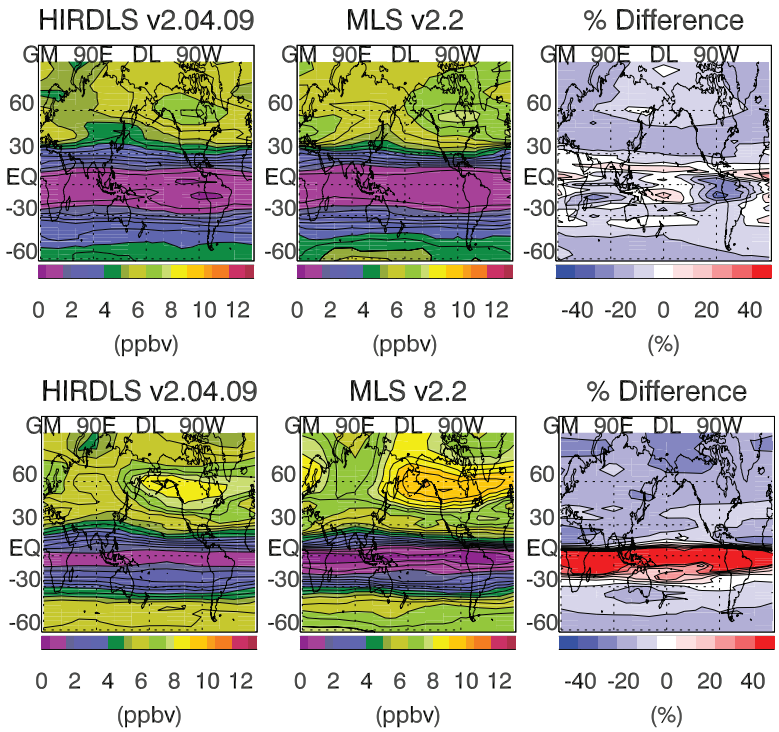


**Figure 8.** Same as Figure 7, except for 3 March 2007.

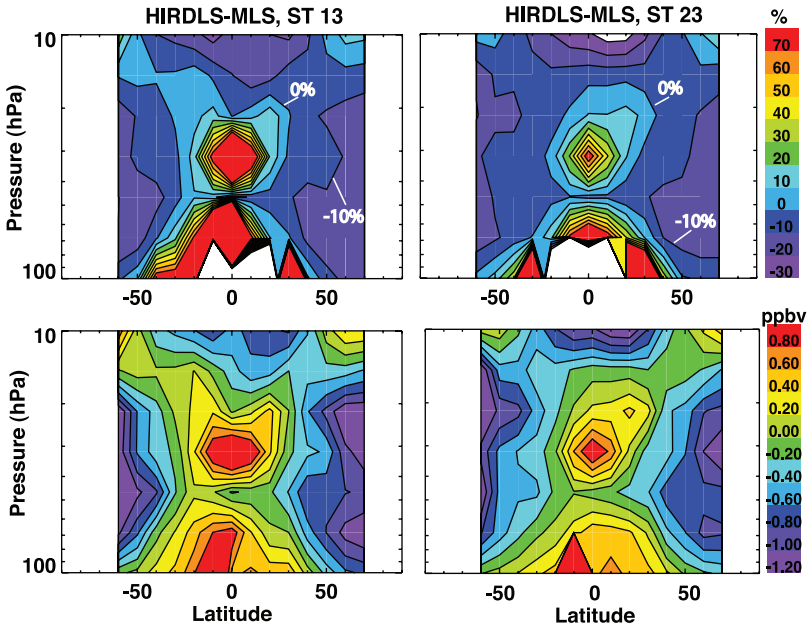


**Figure 9.** Latitude-height cross sections of HIRDLS-MLS coincidences for two different HIRDLS scan tables: (left) scan table 13 and (right) scan table 23. There were 165,513 and 67,595 coincidences used to create the plots for scan tables 13 and 23, respectively. (top) Percentage difference of (HIRDLS − MLS / MLS). (bottom) Absolute differences in volume mixing ratio units (ppbv). See text for details on how the coincidence differences were determined and binned for this figure.

bias become more negative as the pressure increases (lower in altitude), with HIRDLS $HNO_3$ being biased low relative to ACE-FTS $HNO_3$ by 35% and 45% at 100 hPa and 200 hPa, respectively.

## 5. UTLS Region

[32] This section gives an exploratory look into the value of HIRDLS $HNO_3$ observation in the Upper Troposphere and Lower Stratosphere (UTLS). Section 5.1 shows comparisons of HIRDLS $HNO_3$ data with aircraft in situ data measured along the HIRDLS orbit track. Section 5.2 shows the first results of $HNO_3$ filaments as measured by the HIRDLS instrument. The goal of this section is to show the potential value of HIRDLS $HNO_3$ observations in the UTLS region, it is not meant to show quantitative validation of HIRDLS $HNO_3$ in this region.

### 5.1. Comparison to in Situ Observations During Houston AVE

[33] The Chemical Ionization Mass Spectrometer (CIMS) instrument has flown in multiple high-altitude aircraft campaigns [e.g., *Gao et al.*, 2004; *Popp et al.*, 2004, 2006]. For this comparison, only gas-phase $HNO_3$ CIMS data is considered. During the flights examined in this study, the CIMS $HNO_3$ is reported as 1-s averages. This instrument measures $HNO_3$ with an accuracy of ±25%. The accuracy is based on estimates of systematic errors in the instrument inlet flow and nitric acid calibration. The precision (1-$\sigma$) is ±40 pptv for data averaged to 1-s at 50 pptv abundance. The precision estimate is based on analysis of the statistical counting noise in measurements made when the $HNO_3$ mixing ratio is relatively constant. The CIMS instrument has been described in detail by *Neuman et al.* [2000] and *Marcy et al.* [2005].

[34] For this study we have examined two NASA 2005 Houston AVE flights. The coincidences for these two flights are along or near the HIRDLS orbit track. The first flight we will discuss took place on 11 June 2005 (Figure 13). This flight originated from Houston around 1630 UT and flew east over northern Florida and into Georgia. The NASA WB57 aircraft trajectory flew directly over the center of tropical storm Arlene. On the return trip back to Houston, the NASA WB57 aircraft performed a dive and subsequent ascent (near 1900 UT) coincident with the HIRDLS orbital track (see Figure 13, top, between points 1 and 2). During the dive and ascent the WB57 went from 70 hPa down to 175 hPa and then back up to 72 hPa. The latitude for this dive and return to altitude was between 31.68 and 32.83°N. The WB57 UT range was from 1836 to 1927 UT. The magnitude of the CIMS $HNO_3$ data during the dive and ascent varied from approximately 2 ppbv to less than 0.1 ppbv. In Figure 13, bottom, the CIMS $HNO_3$ data along with the mean of three coincident HIRDLS $HNO_3$ profiles are shown. The average HIRDLS UT and total number of coincident profiles are also listed. As mentioned previously, only HIRDLS $HNO_3$ data that had a theoretical precision of $\leq$30% are used. If the criterion is not met at any given HIRDLS retrieval pressure, the data are not used in the mean profile. All the data for each profile are used unless there is a number beside the HIRDLS observation point, in which case this denotes the number of observations used in the mean. The error bars at each HIRDLS retrieval point in the figure are ± the standard deviation (1-$\sigma$) of the HIRDLS measurement. The HIRDLS data are within the

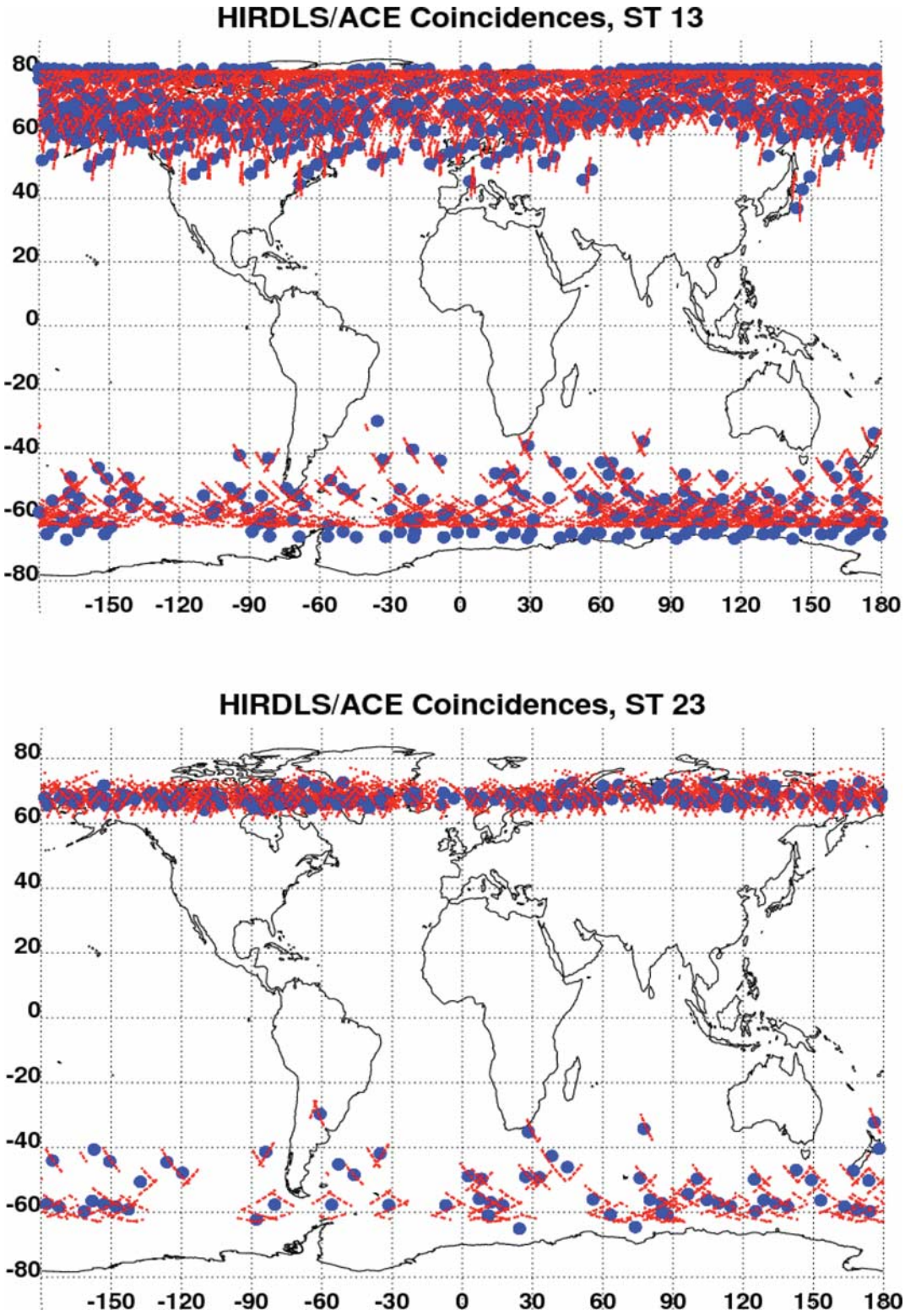


**Figure 10.** Latitude-longitude cross sections showing ACE-FTS $HNO_3$ measurement locations (blue) and HIRDLS $HNO_3$ measurement locations (red). Coincidences are defined as occurring within 2 h in time and 500 km. The coincidences shown here are for two scan tables. (top) Scan table 13. There were 512 coincidences between 23 May 2005 and 15 April 2006 used in this image. (bottom) Scan table 23. There were a total of 150 coincidences between 19 May 2006 and 31 October 2006. See text for details.

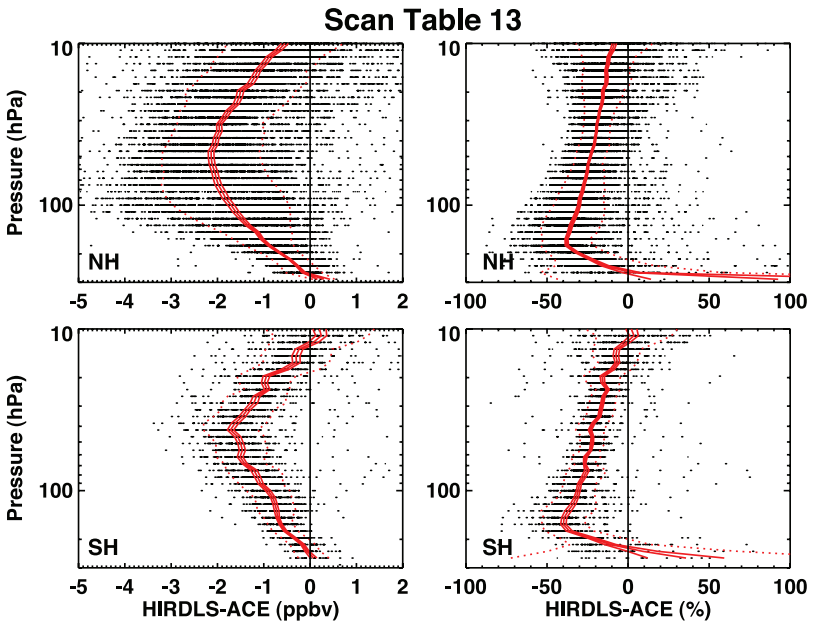


**Figure 11.** Profile differences of HIRDLS and ACE-FTS for the scan table 13 measurements shown in Figure 10. Coincident HIRDLS profiles were averaged together and then subtracted from a single ACE-FTS profile. (top) Percentage difference of (HIRDLS – ACE-FTS / ACE-FTS). (bottom) Absolute differences in volume mixing ratio (ppbv). The mean (solid red line) and standard deviation (dashed red line) of the differences for all coincidences are shown. The individual differences from which these are derived are the horizontally distributed layers of small black dots. The thin red lines bracketing the mean are the uncertainty in the mean (standard deviation divided by the square root of the number of points).

same latitude range of the NASA WB57 profile, but the UT time is later, near 2019 UT. At pressures between 100 hPa and 75 hPa, the HIRDLS $HNO_3$ is consistent with the CIMS $HNO_3$, that is, at the HIRDLS retrieval profiles points, the standard deviation about the mean of the HIRDLS coincident profiles includes the CIMS $HNO_3$ data. At pressures greater than 100 hPa, down to 161 hPa, the HIRDLS $HNO_3$ profile is similar in shape, but biased higher than the CIMS $HNO_3$ data. It is interesting to note that the CIMS instrument observes large variability in $HNO_3$ (0.6 to 1.9 ppbv) when the aircraft is flying at a constant pressure altitude (near 75 hPa; 1836–1827 UT). This observed variability in

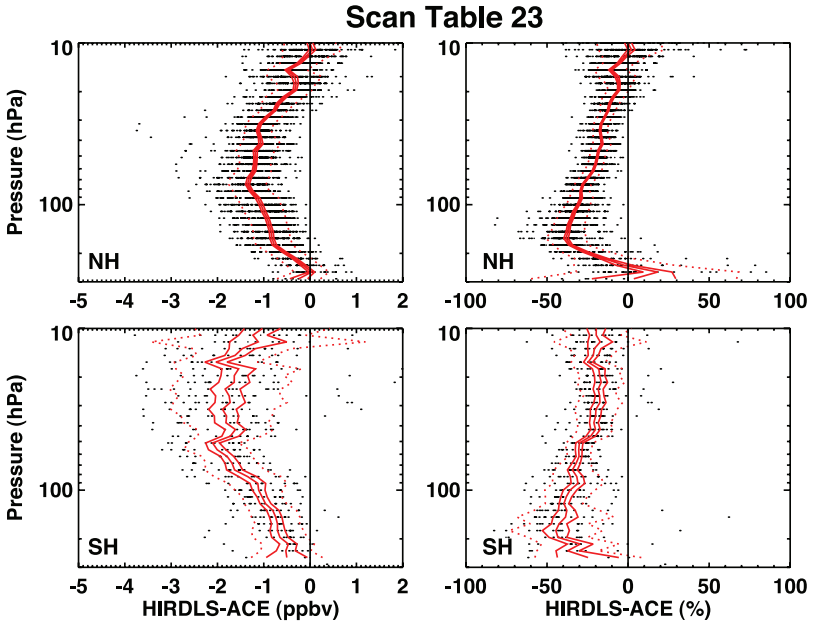


**Figure 12.** Same as Figure 11, except scan table 23 coincident differences are shown.

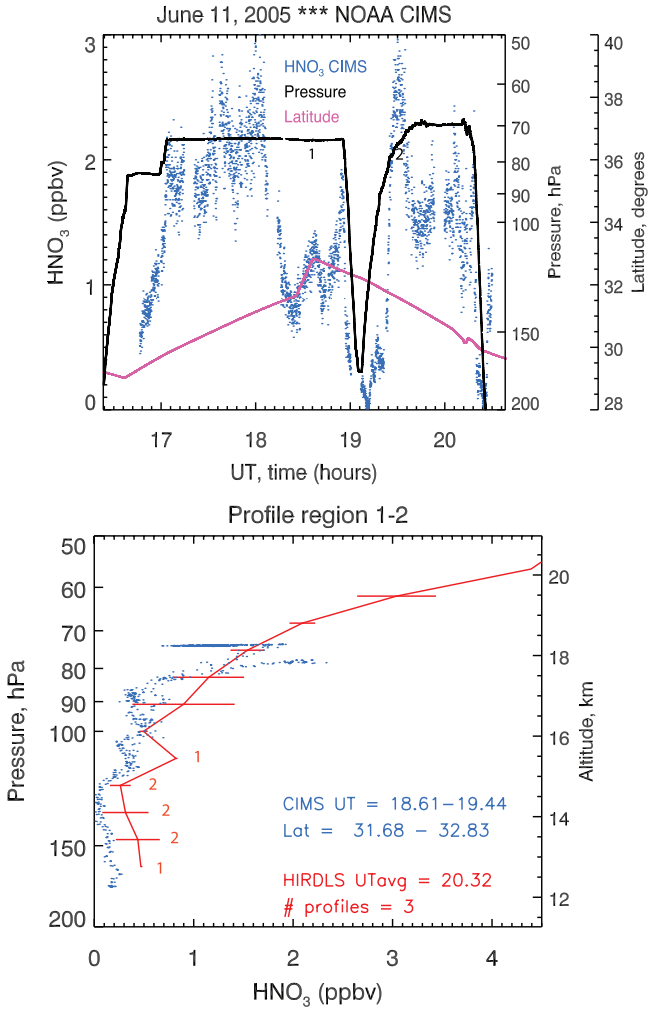


**Figure 13.** Houston AVE flight on 11 June 2005. (top) Observations of in situ $HNO_3$ (ppbv) is shown from the NOAA CIMS instrument (blue). The solid black line is the aircraft pressure altitude. The magenta line is the latitude of the measurements. The aircraft dives and climbs back to altitude between points labeled 1 and 2. This latitude and longitude region between points labeled 1 and 2 is coincident with an ascending HIRDLS orbit. (bottom) Profile comparisons of HIRDLS (red) and NOAA CIMS (blue) $HNO_3$ in volume mixing ratio (ppbv). The CIMS observations are taken between 31.7° and 32.8° latitude, for between 1836 and 1927 UT. There are three HIRDLS $HNO_3$ profiles between 31° and 33° latitude (near 83.4°W longitude) used to create the mean profile. The HIRDLS $HNO_3$ error bars represent the standard deviation (1-$\sigma$) of the three profiles used. See text for details.

$HNO_3$ is over a narrow latitude range (~0.5°). This suggests that one needs to be very careful in drawing conclusions when making coincident data comparisons between satellite and in situ instruments. That is, are the satellite and in situ instruments measuring the same air mass in a region of large horizontal variability? This issue will be discussed in more detail below.

[35] To compare further the HIRDLS $HNO_3$ data with in situ aircraft observations in the lower stratosphere we examined another flight during the 2005 Houston AVE campaign. This flight had multiple dives and ascents along the HIRDLS orbit track. In Figure 14 the flight pattern for 17 June 2005 is shown. This flight took off out of Houston and flew west until it intersected the HIRDLS orbit track at approximately 1806 UT. The aircraft then flew north along the HIRDLS orbit track until 2009 UT. The HIRDLS tangent points for this flight are also shown in Figure 1 (ascending orbit). The latitude range along this flight segment was between 28.5°N to 40°N. At the 2009 UT time, the WB57 flew south back along the same HIRDLS orbit track. The trajectory yielded four profiles for comparison to HIRDLS. The NOAA CIMS data for each profile are shown in blue in Figure 15 along with the mean and standard deviation of the coincident HIRDLS profiles. The CIMS UT and latitude range are listed in the figure legend for each profile region. The HIRDLS $HNO_3$ is also

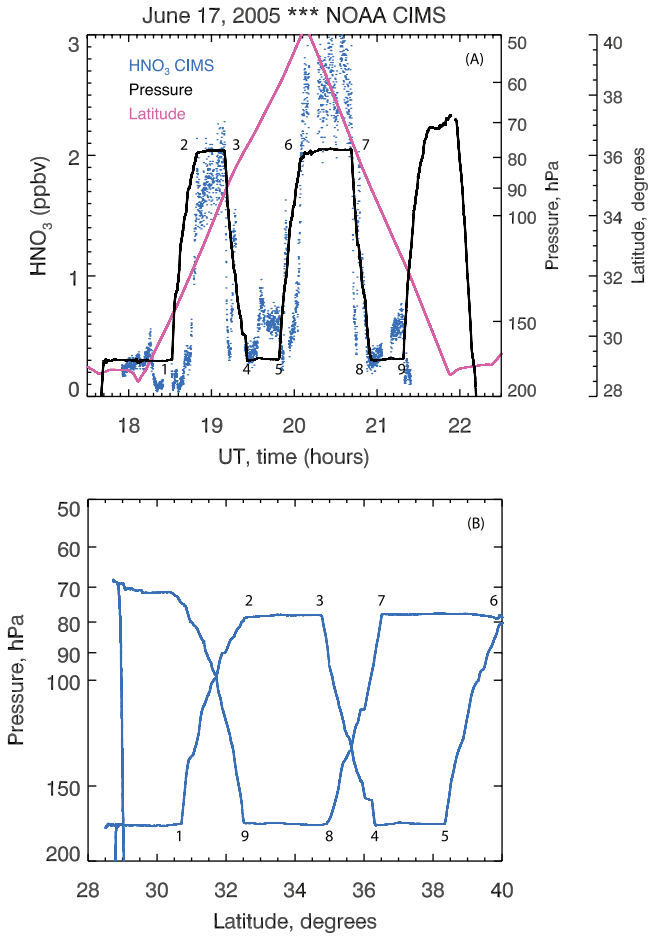


**Figure 14.** Houston AVE flight on 17 June 2005. (top) Observations of in situ $HNO_3$ (ppbv) from the NOAA CIMS instrument (blue). The solid black line is the aircraft pressure altitude. The magenta line is the latitude of the measurements. The aircraft has multiple dives and climbs between points labeled 1 and 2; 3 and 4; 5 and 6; and 7 and 8. The latitude region between UT = 1806 and UT = 2154 follows the HIRDLS ascending orbital track. This track is also shown in Figure 1. (bottom) Latitude-height trajectory of the aircraft for this flight.

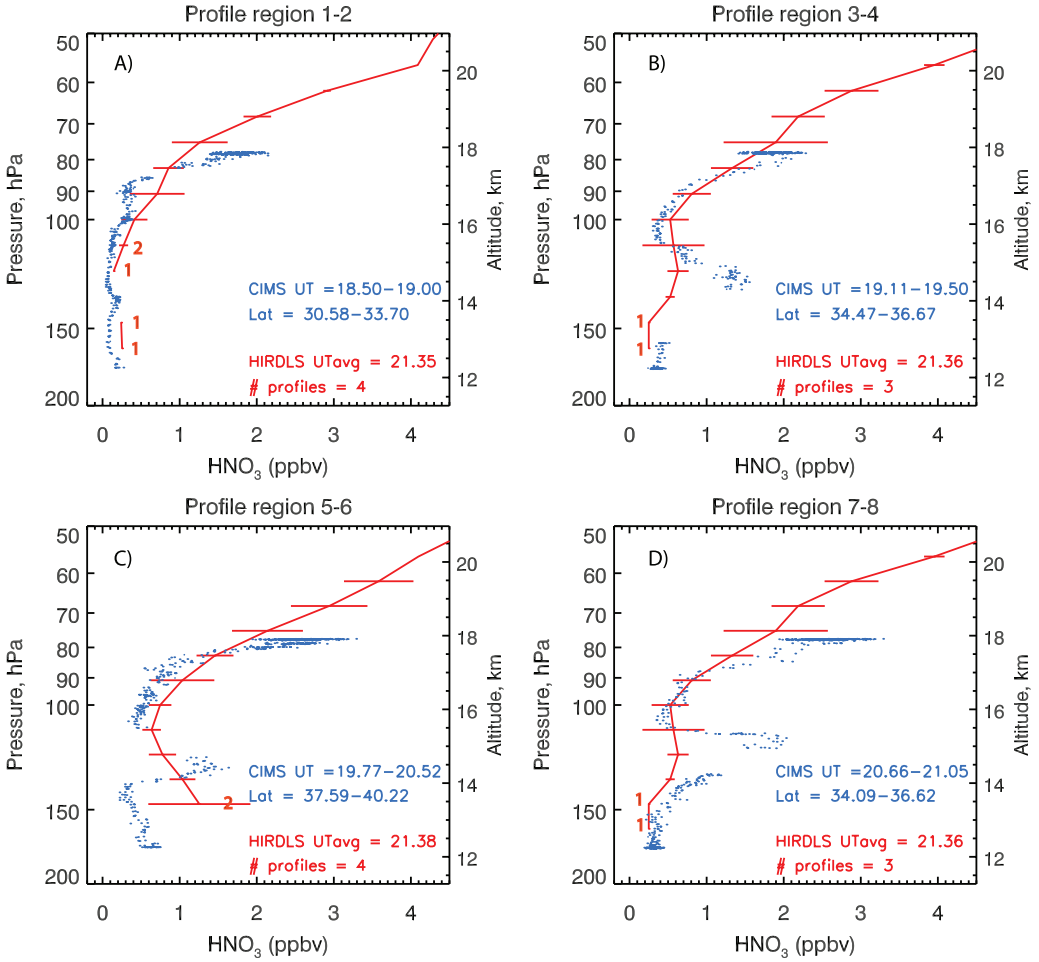


**Figure 15.** Profile comparisons of HIRDLS (red) and NOAA CIMS (blue) $HNO_3$ (ppbv). The four profile regions shown in Figure 14 are displayed. The UT and latitude range of the CIMS data is listed in each plot. Coincident HIRDLS profiles are only taken between the given CIMS latitude ranges. The numbers of HIRDLS profiles for this latitude range are listed in each plot. The HIRDLS $HNO_3$ error bars represent the standard deviation (1-$\sigma$) of the profiles used in the mean. See text for details.

consistent with the CIMS $HNO_3$ in the 100 hPa to 75 hPa range in the four profiles regions shown in Figure 15. However, the HIRDLS data does not capture the $HNO_3$ filament between 100 hPa and 150 hPa observed by CIMS in Figures 15b and 15d. The $HNO_3$ filament in profile regions 3–4 and 7–8 is most likely the same, with profile region 3–4 sampling this air mass approximately 1.5 h earlier than profile region 7–8. In Figure 15c, profile region 5–6 (near 39°N), the HIRDLS mean profile does show elevated values. We have examined a latitude-height cross section of $HNO_3$ along the HIRDLS orbit track (not shown) and do see large abundance of $HNO_3$ between 38 and 40°N and 150–100 hPa, consistent with the filament measured by CIMS. However, in Figures 15b and 15d, profile regions 3–4 and 7–8 (near 35°N), there is less of an indication that HIRDLS is measuring the $HNO_3$ filaments as measured by CIMS. There are two possible reasons why the HIRDLS instrument does not measure these two $HNO_3$ filaments. The first is that this is a localized event and the HIRDLS viewing geometry along the limb is not aligned correctly to pick up this feature. The location of this filament is near the tropopause and when one examines the potential vorticity gradients from meteorological analysis (not shown), the horizontal and temporal variability is large at the altitude of observed filament peak. Therefore, it is possible that HIRDLS instrument is not measuring the same air mass as the CIMS instrument. The vertical resolution of the HIRDLS instrument also makes it difficult to measure a $HNO_3$ filament in this region of the atmosphere. For example, if we focus on the filament for profile region 7–8, the vertical scale of this filament at half maximum amplitude is approximately 1 km, and the amplitude of the peak $HNO_3$ mixing ratio is near 15 km (120 hPa). In Figure 16 the HIRDLS $HNO_3$ averaging kernels and FWHM resolution are shown for this orbit segment at 35.2°N. The FWHM resolution goes from 2.5 km at 12 km, to 1.1 km at 17 km. The vertical resolution near 15 km is approximately 1.5 km, which is coarser than the vertical scale of the $HNO_3$ filament as measured by CIMS. Therefore, it is likely that the HIRDLS instrument cannot resolve a 1 km feature in this region of the atmosphere. Future work will investigate additional NASA AVE missions to better characterize the

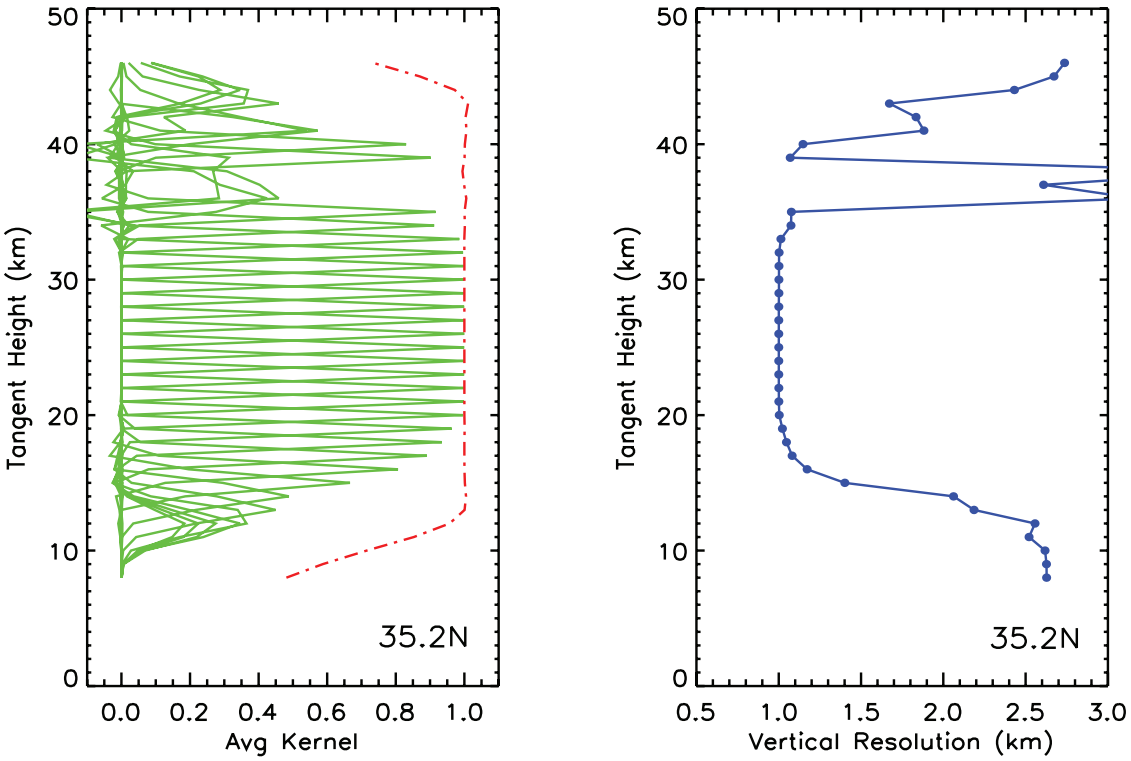


**Figure 16.** HIRDLS $HNO_3$ averaging kernels and full-width half-maximum (FWHM) vertical resolution are shown on 17 June 2005 at 35.2°N. (left) Averaging kernels (green lines) and the integrated area under each kernel (red line). (right) Vertical resolution as derived from the FWHM of each kernel (blue line).

limits of the HIRDLS $HNO_3$ measurements in the UTLS region.

### 5.2. HIRDLS $HNO_3$ Filaments

[36] Episodic intrusions of synoptic-scale filaments of stratospheric air into the upper troposphere, commonly known as 'tropopause folding' events, are an important mechanism for irreversible stratosphere-troposphere exchange (STE) [*Holton et al.*, 1995, and the reference within]. In this section, we show that HIRDLS observes a $HNO_3$ filament that is consistent with the idea that stratospheric air rich in $HNO_3$ is transported into the UTLS region, specifically in the region commonly called the middle world [*Holton et al.*, 1995].

[37] In Figure 17, a HIRDLS Northern Hemisphere descending orbit segment on 10 March 2006, approximately 0100 UT, is shown. This segment extends from approximately 70°N, 19°W to 10°N, 10°W. Between 40°N and 50°N, 8°W, a synoptic-scale event is observed as shown in Figure 18. Figure 18 (top) shows the potential vorticity (PV) data product as derived from the National Centers for Environmental Prediction (NCEP) Global Forecast System (GFS) Final Global Data Assimilation System (FNL). This assimilation system has a horizontal resolution of 1° with 26 vertical levels from the surface to 10 hPa. See *Pan et al.* [2007] for more discussion of this meteorological data product. The NCEP GFS 0 UT meteorological products were interpolated to the HIRDLS tangent point locations as shown in Figure 17. Figure 18 (top) shows a large PV intrusion (i.e., filament) of stratospheric air extending into the middle world between 40°N and 50°N. The white lines are the NCEP GFS horizontal winds for this orbit section. The horizontal winds are defined as the $(V^2 + U^2)^{1/2}$, where V and U are the meridional and zonal winds from NCEP GFS. The 3 pvu (1 pvu = $10^{-6}$ K $m^2$ $kg^2$ $s^{-1}$) contour line is highlighted as a solid black line; this contour line is also shown Figure 18 (middle and bottom). In addition the NCEP

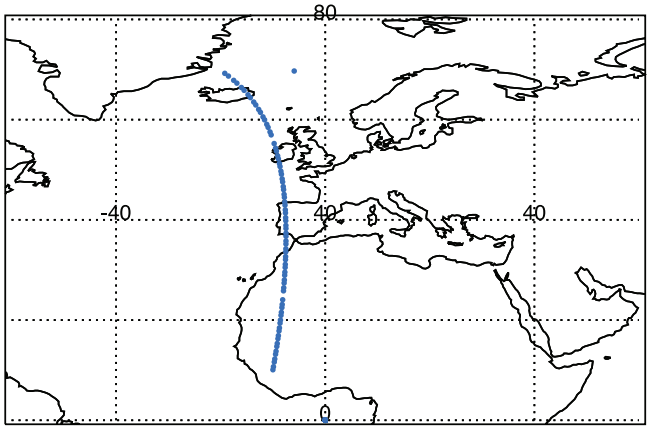


**Figure 17.** Latitude-longitude cross sections showing HIRDLS profile tangent point locations for a descending orbit on 10 March 2006.

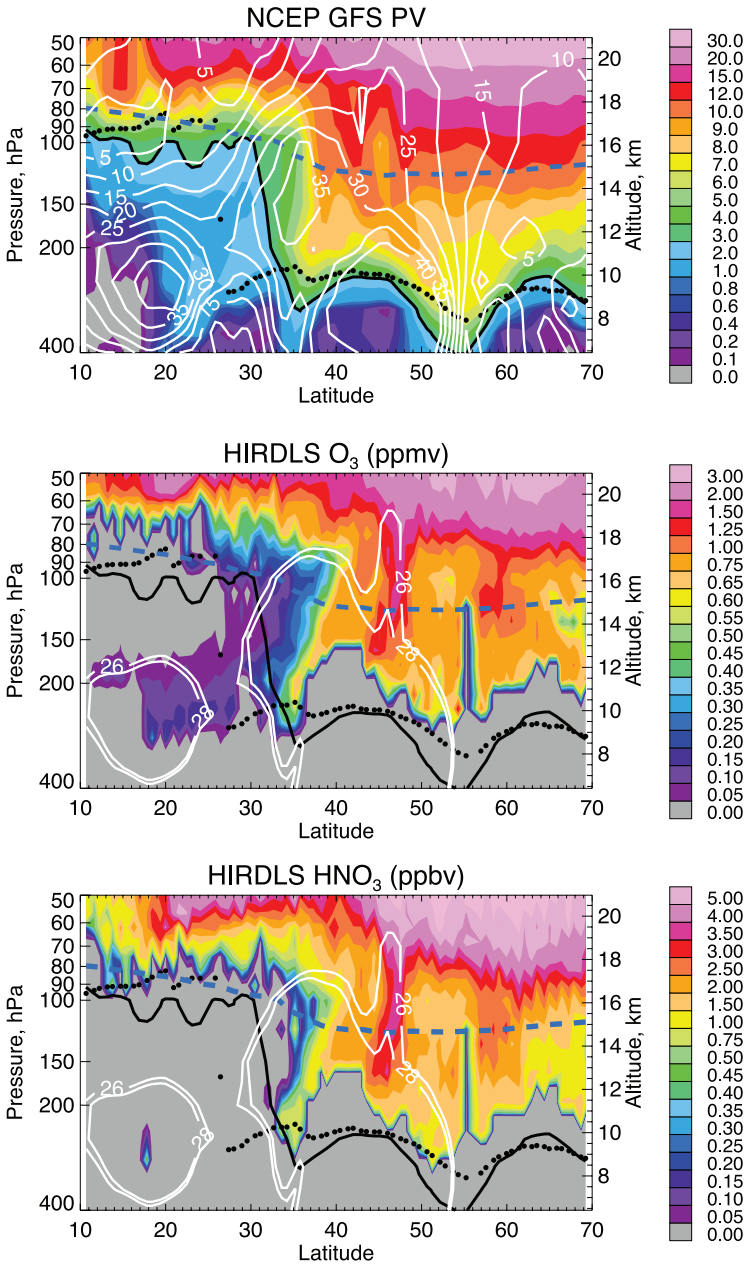


**Figure 18.** Latitude-height comparisons of meteorological products from the NCEP GFS and HIRDLS $O_3$ and $HNO_3$ data products for the orbit segment shown in Figure 17. (top) Color contours of potential vorticity; the solid black line is for the 3 pvu contour. Horizontal wind contours are shown in white (for every 5 m $s^{-1}$). The 400 K potential temperature contour is shown as a blue dashed line. The tropopause pressure altitude is shown as filled black circles. Color contours of (middle) HIRDLS $O_3$ (ppmv) and (bottom) $HNO_3$ (ppbv). The white contour lines are the horizontal wind contours for 26 and 28 m $s^{-1}$.

GPS tropopause pressure is shown. Between approximately 30°N and 70°N the tropopause is between 9 and 10 km for this orbit segment. The blue dashed line in Figure 18 is the 400 K potential temperature contour. The region between the 400 K line and 3 pvu line is commonly called the middle world. In Figure 18 (middle), HIRDLS $O_3$ is shown in volume mixing ratio units. The image shows that HIRDLS observes an $O_3$ filament in the same region as the NCEP GPS intrusion. The magnitude of the HIRDLS $O_3$ filament is approximately 1.25 ppmv between 40°N and 50°N near 150 hPa (~13 km). In this pressure region, but outside this latitude range, the HIRDLS $O_3$ abundance is approximately half the observed abundance in the center of the filament. In Figure 18 (bottom), HIRDLS $HNO_3$ is also shown along the same orbit segment. There is a clear coincidence of high HIRDLS $HNO_3$ in the same region where there are high values of NCEP GFS PV and HIRDLS $O_3$. The HIRDLS $HNO_3$ filament between 40°N and 50°N and 150 hPa (~13 km) shows abundances of $HNO_3$ near 3 ppbv, consistent with values of $HNO_3$ originating higher up in the

**Table 1.** Vertical Resolution Estimates and Summary of Comparisons of HIRDLS Version 2.04.09 $HNO_3$ Data Product to Correlative Observations

| | UTLS Region | 100–10 hPa Equatorial 20°S–20°N | 100–10 hPa Midlatitudes 20°N, S–50°N, S | 100–10 hPa Polar 50°S–60°S; 50°N–80°N |
|---|---|---|---|---|
| HIRDLS Vertical Resolution | Strongly dependent on latitude and altitude. Can range from 1 to >2.5 km (Figure 16) | Approximately 1.0 km (Figure 2) | Approximately 1.0 km (Figure 2) | Approximately 1.0 km (Figure 2) |
| MLS/Aura Satellite Data version 2.2 | NA | HIRDLS is biased high relative to MLS near 30 hPa (∼50%). See Figures 6–9. The coincident differences between HIRDLS and MLS are worse with ST13 (relative to ST23). | Horizontal and vertical structure is consistent with MLS (Figures 6–8). HIRDLS is biased ∼10% low (Figure 9). Both HIRDLS scan tables give similar results. | HIRDLS is biased ∼10% low (Figure 9). Both HIRDLS scan tables give similar results. |
| ACE-FTS/SCISAT-1 satellite Data version 2.2 | In the high-latitude region, at pressures between 100 and 200 hPa, HIRDLS is biased low by 30–40% (Figures 11 and 12). | NA | The comparisons with ACE-FTS were mostly >50°N,S (Figure 10). | The HIRDLS ACE-FTS coincident differences were similar between ST13 and ST23. HIRDLS Is biased low by 0–30% depending on altitude (Figures 11 and 12). |
| NOAA CIMS in situ instrument on the WB57 NASA AVE Fights | Profiles of HIRDLS and CIMS overlap within HIRDLS variability error bars (Figure 15). HIRDLS does not resolve 1-km FWHM filaments as measured by CIMS (Figures 15 and 16). | NA | See comments in UTLS region. | NA |
| NCEP GFS Meteorological Analysis | HIRDLS observed $HNO_3$ filaments along an orbit segment consistent with Met. Analysis and HIRDLS $O_3$ (Figure 18). | NA | See comments in UTLS region. | NA |

stratosphere. Both the $O_3$ and $HNO_3$ filaments are perpendicular to the 400 K potential temperature surface and penetrate deep into the middle world. To highlight that the $O_3$ and $HNO_3$ filament as observed by HIRDLS is a real feature that is dynamically influenced, the horizontal wind fields are also overlaid on Figures 18 (middle and bottom). The horizontal wind field contours of 26 and 28 m/s are chosen to highlight the dynamical feature near the $O_3$ filament. It is clear from viewing Figure 18 that there is deformation of the horizontal wind structure coincident with the observed HIRDLS $O_3$ and $HNO_3$ filaments. Figure 18 shows just one example of $O_3$ and $HNO_3$ filament structure; additional examples have been documented in the HIRDLS data record and will be the focus of future investigations. However, it is clear from this work that HIRDLS is able to observe synoptic-scale $HNO_3$ filaments in the UTLS region.

## 6. Summary and Conclusions

[38] We have shown the first observations of $HNO_3$ (version 2.04.09) from the HIRDLS instrument on the EOS Aura satellite. In this paper we have focused primarily on the region of the atmosphere between 100 hPa and 10 hPa, and examined HIRDLS data from 28 April 2005 to present. This period is operationally defined by the use of scan tables 13, 22, and 23. HIRDLS $HNO_3$ results are consistent across scan tables. HIRDLS observations before 28 April 2005 are marginal in quality and were not discussed in this work. We also did not show results for HIRDLS $HNO_3$ at pressures <10 hPa (higher in altitude). This region is characterized by high theoretical precision (typically >30%) and will be examined in future validation studies. We also focused on the midlatitude UTLS region. Comparisons were made with an in situ $HNO_3$ instrument during one of the NASA AVE campaigns. We also examined $HNO_3$ filament structure in the middle world and compared to HIRDLS $O_3$ and meteorological analysis for coincident conditions. Table 1 give a summary of the HIRDLS estimated vertical resolution and correlative data comparisons. Below is a brief summary of our findings.

[39] The HIRDLS $HNO_3$ vertical resolution was estimated by examining the HIRDLS $HNO_3$ averaging kernels in different latitude regions. In the 100 hPa to 10 hPa region of the atmosphere, the HIRDLS $HNO_3$ FWHM vertical resolution is approximately 1 km (Figure 2). This resolution can be larger in the UTLS region, approaching 2.5 km (Figure 16).

[40] The HIRDLS $HNO_3$ precision was estimated in two ways. The first approach examined the precision as derived by the HIRDLS level-2 retrieval algorithm. We called this the "theoretical" precision. The second approach derived

the precision by examining HIRDLS $HNO_3$ data in regions of low atmospheric variability. We binned the HIRDLS data onto equivalent latitude–potential temperature grid to further reduce geophysical variability. We called this the "measured" precision. The theoretical precision estimate showed that between 100 and 10 hPa, the theoretical precision was typically 5–10% (Figures 3 and 4). This value increased sharply for pressures <10 hPa (higher in altitude) and >100 hPa (lower in altitude). For all correlative data comparisons in this study, we only used HIRDLS $HNO_3$ data that had a theoretical precision of $\leq$30%. This is a conservative approach, but it does minimize any random error contribution from the a priori estimate and other error sources (Figure 2). The second precision estimate, the measured precision, not only includes errors from the retrieval approach, but also contributions from atmospheric variability (even though we did try to minimize this variability). Here we found the observed precision to be approximately 10–15% in the 100 hPa to 10 hPa pressure range (Figure 5).

[41] The HIRDLS $HNO_3$ distributions show global and seasonal structure that is consistent with our current understanding of the seasonal distributions of $HNO_3$ in the stratosphere. We made comparisons to the EOS Aura MLS instrument and found that under similar temporal and geographic conditions the synoptic-scale structure is consistent between the two instruments. We also made coincident comparisons with the Aura MLS $HNO_3$ and found that outside of the tropics, HIRDLS was biased approximately 0–20% low (Figures 6–9). In the tropics, HIRDLS was biased 50% high near 30 hPa. More work will be needed to see whether this high bias in the tropics is an issue with the HIRDLS or Aura MLS $HNO_3$ observations.

[42] We found that HIRDLS $HNO_3$ was also biased low relative to the ACE-FTS instruments. Statistical comparisons to ACE-FTS were made primarily in high-latitude regions in both the Northern and Southern Hemispheres and the low bias is typically between 10 and 30% in the 100 hPa to 10 hPa pressure range (Figures 10–12). It should be mentioned that *Santee et al.* [2007] compared Aura MLS to ACE-FTS $HNO_3$ and found that Aura MLS $HNO_3$ were biased low to ACE-FTS by approximately 10%.

[43] We also examined HIRDLS $HNO_3$ abundances in the midlatitude, UTLS region. Here, we compared HIRDLS $HNO_3$ to in situ data from the NOAA CIMS instrument during the 2005 NASA Houston AVE campaign (Figures 13–15). Comparisons were made when the CIMS instrument was flown on the NASA WB57 aircraft near or along the HIRDLS orbital track. Although in this case we did not attempt a quantitative comparison between the coincident HIRDLS/CIMS measurements, the error bars of the mean HIRDLS $HNO_3$ profile typically overlap the CIMS $HNO_3$ data. However, for two profiles shown in section 5.1, HIRDLS was not sensitive to high $HNO_3$ abundances contained in filaments that were observed by the CIMS instrument during aircraft descents. These filaments (most likely the same air mass) had a vertical scale at half maximum of approximately 1 km. Meteorological analysis suggested that there is large horizontal and temporal variability in this region of the atmosphere near the peak $HNO_3$ abundance of these filaments. Therefore, it is very likely that the HIRDLS instrument is not measuring the same air mass as the in situ CIMS instrument. In addition, in this latitude and height region of the atmosphere, the averaging kernel derived vertical scale for HIRDLS $HNO_3$ is on the order of 1.5 km (Figure 16). Therefore, one would expect the sharpness of the CIMS $HNO_3$ peak to be "smeared out" when observed by the HIRDLS field-of-view. In future work we plan to make quantitative comparisons with the CIMS data after the CIMS data have been modified by the HIRDLS averaging kernels. We will not only reevaluate the flights on 11 and 17 June 2005, but also additional flights during this NASA Houston AVE campaign and other flights in additional NASA AVE campaigns.

[44] We also showed results of HIRDLS $HNO_3$ filament structure in the middle world. We compared HIRDLS $HNO_3$ to meteorological analysis from the NCEP GFS. We found that a $HNO_3$ filament as observed on 10 March 2006 near 45°N latitude, 8°W longitude is consistent with horizontal wind and PV fields derived from the NCEP GFS. We also showed that the HIRDLS $O_3$ observations showed the same filament structure.

[45] **Acknowledgments.** The authors would like to thank Laura Pan and Rolando Garcia for their helpful comments on this paper. The work discussed in this paper is funded by NASA's Aura satellite program under contract NAS5–97046. Work at the Jet Propulsion Laboratory, California Institute of Technology, was carried out under a contract with the National Aeronautics and Space Administration. The National Center for Atmospheric Research is operated by the University Corporation for Atmospheric Research under the sponsorship of the National Science Foundation. Funding for ACE was provided by the Canadian Space Agency (CSA) and the Natural Sciences and Engineering Research Council (NSERC) of Canada. The CIMS $HNO_3$ measurements were supported by the NASA Upper Atmospheric Research Program and the NOAA Atmospheric Chemistry and Climate Program.

## References

Arnold, F. (1992), Stratospheric aerosol increases and ozone destruction: Implications from mass spectrometer measurements, *Ber. Bunsenges. Phys. Chem.*, *96*, 339–350.

Austin, J., R. R. Garcia, J. M. Russell III, S. Solomon, and A. F. Tuck (1986), On the atmospheric photochemistry of nitric acid, *J. Geophys. Res.*, *91*, 5477–5485, doi:10.1029/JD091iD05p05477.

Bernath, P. F., et al. (2005), Atmospheric Chemistry Experiment (ACE): Mission overview, *Geophys. Res. Lett.*, *32*, L15S01, doi:10.1029/2005GL022386.

Boone, C. D., R. Nassar, K. A. Walker, Y. Rochon, S. D. McLeod, C. P. Rinsland, and P. F. Bernath (2005), Retrievals for the Atmospheric Chemistry Experiment Fourier-transform spectrometer, *Appl. Opt.*, *44*, 7218–7231, doi:10.1364/AO.44.007218.

Brasseur, G. P., and S. Solomon (2005), *Aeronomy of the Middle Atmosphere*, 3rd rev., *Atmos. Oceanogr. Sci. Libr.*, vol. 32, Springer, New York.

Carslaw, K. S., B. P. Luo, S. L. Clegg, T. Peter, P. Brimblecombe, and P. J. Crutzen (1994), Stratospheric aerosol growth and $HNO_3$ gas phase depletion from coupled $HNO_3$ and $H_2O$ uptake by liquid particles, *Geophys. Res. Lett.*, *21*, 2479–2482, doi:10.1029/94GL02799.

Crutzen, P. J. (1971), Ozone production rates in oxygen-hydrogen-nitrogen oxide atmosphere, *J. Geophys. Res.*, *76*, 7311–7327, doi:10.1029/JC076i030p07311.

Crutzen, P. J., and F. Arnold (1986), Nitric acid cloud formation in the cold Antarctic stratosphere: A major cause for the springtime 'ozone hole', *Nature*, *324*, 651–655, doi:10.1038/324651a0.

Dye, J. E., D. Baumgardner, B. W. Gandrud, S. R. W. Kawa, K. K. Kelly, M. Loewenstein, G. V. Ferry, K. R. Chan, and B. L. Gray (1992), Particle size distributions in Arctic polar stratosphere clouds, growth and freezing of sulfuric acid droplets and implications for cloud formation, *J. Geophys. Res.*, *97*, 8015–8034.

Edwards, D. P., J. C. Gille, P. L. Bailey, and J. J. Barnett (1995), Selection of sounding channels for the High Resolution Dynamics Limb Sounder, *Appl. Opt.*, *34*, 7006–7018.

Fahey, D. W., et al. (2001), The detection of large $HNO_3$-containing particles in the winter Arctic stratosphere, *Science*, *291*, 1026–1031, doi:10.1126/science.1057265.

Francis, G. L., D. P. Edwards, A. Lambert, C. M. Halvorson, J. M. Lee-Taylor, and J. C. Gille (2006), Forward modeling and radiative transfer for the NASA EOS-Aura High Resolution Dynamics Limb Sounder (HIRDLS) instrument, *J. Geophys. Res.*, *111*, D13301, doi:10.1029/2005JD006270.

Gao, R. S., et al. (2004), Evidence that nitric acid increases relative humidity in low-temperature cirrus clouds, *Science*, *303*, 516–520, doi:10.1126/science.1091255.

Gille, J. C., and J. J. Barnett (1992), The High Resolution Dynamics Limb Sounder (HIRDLS), An instrument for the study of global change, *Rend. Sc. Int. Fis.*, *CXV*, 433–450.

Gille, J. C., and J. J. Barnett (1996), Conceptual design of the High Resolution Dynamics Limb Sounder (HIRDLS), *Proc. SPIE Int. Soc. Opt. Eng.*, *2830*, 190–201, doi:10.1117/12.256115.

Gille, J. C., and F. B. House (1971), On the inversion of infrared limb emission measurements, I. Temperature and thickness, *J. Atmos. Sci.*, *28*, 1427–1442, doi:10.1175/1520-0469(1971)028<1427:OTIOLR>2.0.CO;2.

Gille, J. C., and M. M. Russell III (1984), The Limb Infrared Monitor of the Stratosphere: Experiment description, performance, and results, *J. Geophys. Res.*, *89*, 5125–5140, doi:10.1029/JD089iD04p05125.

Gille, J. C., P. L. Bailey, R. A. Craig, F. B. House, and G. P. Anderson (1980), Sounding the stratosphere and mesosphere by infrared limb scanning from space, *Science*, *208*, 397–399, doi:10.1126/science.208.4442.397.

Gille, J. C., et al. (1984), Accuracy and precision of the nitric acid concentration determined by the Limb Infrared Monitor of the Stratosphere experiment on the Nimbus 7, *J. Geophys. Res.*, *89*, 5179–5190, doi:10.1029/JD089iD04p05179.

Gille, J. C., P. L. Bailey, and C. A. Craig (1987), Proposed reference model for nitric acid, *Adv. Space Res.*, *7*, 25–35, doi:10.1016/0273-1177(87)90247-X.

Gille, J. C., P. L. Bailey, and C. A. Craig (1993), Revised reference model for nitric acid, *Adv. Space Res.*, *13*, 59–72, doi:10.1016/0273-1177(93)90007-X.

Gille, J. C., L. V. Lyjak, P. L. Bailey, A. E. Roche, J. B. Kumer, and J. L. Mergenthaler (1998), Update to the stratospheric nitric acid reference atmosphere, *Adv. Space Res.*, *7*, 925–935.

Gille, J. C., et al. (2005), Development of special corrective processing of HIRDLS data and early validation, in *Infrared Space Borne Remote Sensing 2005*, edited by M. Strojnik, *SPIE 5883*, SPIE-Int. Soc. for Opt. Eng., Bellingham, Wash.

Gille, J. C., et al. (2008), The High Resolution Dynamics Limb Sounder (HIRDLS): Experiment overview, recovery, and validation of initial temperature data, *J. Geophys. Res.*, doi:10.1029/2007JD008824, in press.

Hofmann, D. J., and S. Solomon (1989), Ozone destruction through heterogeneous chemistry following the eruption of El Chicón, *J. Geophys. Res.*, *94*, 5029–5041, doi:10.1029/JD094iD04p05029.

Holton, J. R., P. H. Haynes, M. E. McIntyre, A. R. Douglass, R. B. Rood, and L. Pfister (1995), Stratosphere-troposphere exchange, *Rev. Geophys.*, *33*, 403–439.

Höpfner, M., et al. (2006), Spectroscopic evidence for NAT, STS, and ice in MIPAS infrared limb emission measurements of polar stratospheric clouds, *Atmos. Chem. Phys.*, *6*, 1201–1219.

Irie, H., et al. (2006), Validation of stratospheric nitric acid profiles observed by Improved Limb Atmospheric Spectrometer (ILAS)-II, *J. Geophys. Res.*, *111*, D11S03, doi:10.1029/2005JD006115.

Johnston, H. S. (1971), Reduction of stratospheric ozone by nitrogen oxide catalysts from supersonic transport exhaust, *Science*, *173*, 517–522, doi:10.1126/science.173.3996.517.

Kinnison, D. E., et al. (2007), Sensitivity of chemical tracers to meteorological parameters in the MOZART-3 chemical transport model, *J. Geophys. Res.*, *112*, D20302, doi:10.1029/2006JD007879.

Koike, M., et al. (2000), A comparison of Arctic $HNO_3$ profiles measured by the Improved Limb Atmospheric Spectrometer and balloon-borne sensors, *J. Geophys. Res.*, *105*, 6761–6771, doi:10.1029/1999JD901057.

Lambert, A., P. L. Bailey, D. P. Edwards, J. C. Gille, B. R. Johnson, C. M. Halvorson, S. T. Massie, and K. A. Stone (1999), High-Resolution Dynamics Limb Sounder, Level-2 algorithm theoretical basis document, report, Atmos. Oceanic, and Planet. Phys., Univ. of Oxford, Oxford, U.K. (Available at http://www.atm.ox.ac.uk/group/hirdls/doc/sw/hirdls_lvl2_atbd_v2.pdf)

Marcy, T. P., R. S. Gao, M. J. Northway, P. J. Popp, H. Stark, and D. W. Fahey (2005), Using chemical ionization mass spectrometry for detection of $HNO_3$, HCl, and $ClONO_2$ in the atmosphere, *Int. J. Mass Spectrom.*, *243*, 63–70, doi:10.1016/j.ijms.2004.11.012.

Mengistu Tsidu, G., et al. (2005), $NO_y$ from Michelson Interferometer for Passive Atmospheric Sounding on Environmental Satellite during the Southern Hemisphere polar vortex split in September/October 2002, *J. Geophys. Res.*, *110*, D11301, doi:10.1029/2004JD005322.

Neuman, J. A., et al. (2000), A fast-response chemical ionization mass spectrometer for in situ measurements of $HNO_3$ in the upper troposphere and lower stratosphere, *Rev. Sci. Instrum.*, *71*(10), 3886–3892, doi:10.1063/1.1289679.

Pan, L. L., W. J. Randel, H. Nakajima, S. T. Massie, H. Kanzawa, Y. Sasano, T. Yokota, T. Sugita, S. Hayashida, and S. Oshchepkov (2002), Satellite observations of dehydration in the Arctic Polar stratosphere, *Geophys. Res. Lett.*, *29*(8), 1184, doi:10.1029/2001GL014147.

Pan, L. L., et al. (2007), Chemical behavior of the tropopause observed during the Stratospheric-Troposphere Analyses of Regional Transport experiment, *J. Geophys. Res.*, *112*, D18110, doi:10.1029/2007JD008645.

Popp, P. J., et al. (2004), Nitric acid uptake on subtropical cirrus cloud particles, *J. Geophys. Res.*, *109*, D06302, doi:10.1029/2003JD004255.

Popp, P. J., et al. (2006), The observation of nitric acid-containing particles in the tropical lower stratosphere, *Atmos. Chem. Phys.*, *6*, 601–611.

Roche, A. E., J. B. Kumer, J. L. Mergenthaler, R. W. Nightingale, W. G. Uplinger, G. A. Ely, and J. F. Potter (1994), Observations of lower-stratospheric $ClONO_2$, $HNO_3$, and aerosol by the UARS CLAES experiment between January 1992 and April 1993, *J. Atmos. Sci.*, *51*, 2877–2902, doi:10.1175/1520-0469(1994)051<2877:OOLSCH>2.0.CO;2.

Rodgers, C. D. (2000), *Inverse Methods for Atmospheric Sounding, Theory and Practice*, World Sci., Tokyo.

Rothman, L. S., et al. (2003), The HITRAN 2004 molecular spectroscopic database: Edition of 2000 including updates through 2001, *J. Quant. Spectrosc. Radiat. Transfer*, *82*, 5–44, doi:10.1016/S0022-4073(03)00146-8.

Santee, M. L., W. G. Read, J. W. Waters, L. Froidevaux, G. L. Manney, D. A. Flower, R. F. Jarnot, R. S. Harwood, and G. E. Peckham (1995), Interhemispheric differences in polar stratospheric $HNO_3$, $H_2O$, ClO, and $O_3$, *Science*, *267*, 849–852, doi:10.1126/science.267.5199.849.

Santee, M. L., G. L. Manney, L. Froidevaux, R. W. Zurek, and J. W. Waters (1997), MLS observations of ClO and $HNO_3$ in the 1996–97 Arctic polar vortex, *Geophys. Res. Lett.*, *24*, 2713–2716, doi:10.1029/97GL52830.

Santee, M. L., A. Tabazadeh, G. L. Manney, R. J. Salawitch, L. Froidevaux, W. G. Read, and J. W. Waters (1998), UARS Microwave Limb Sounder $HNO_3$ observations: Implications for Antarctic polar stratospheric clouds, *J. Geophys. Res.*, *103*, 13,285–13,313, doi:10.1029/98JD00365.

Santee, M. L., G. L. Manney, N. J. Livesey, and J. W. Waters (2000), UARS Microwave Limb Sounder Observations of denitrification and ozone loss in the 2000 Arctic late winter, *Geophys. Res. Lett.*, *27*, 3213–3216, doi:10.1029/2000GL011738.

Santee, M. L., A. Tabazadeh, G. L. Manney, M. D. Fromm, R. M. Bevilacqua, J. W. Waters, and E. J. Jensen (2002), A Lagrangian approach to studying Arctic polar stratospheric clouds using UARS MLS $HNO_3$ and POAM II aerosol extinction measurements, *J. Geophys. Res.*, *107*(D10), 4098, doi:10.1029/2000JD000227.

Santee, M. L., G. L. Manney, N. J. Livesey, and W. G. Read (2004), Three-dimensional structure and evolution of stratospheric $HNO_3$ based on UARS Microwave Limb Sounder measurements, *J. Geophys. Res.*, *109*, D15306, doi:10.1029/2004JD004578.

Santee, M. L., G. L. Manney, N. J. Livesey, L. Froidevaux, I. A. MacKenzie, H. C. Pumphrey, W. G. Read, M. J. Schwartz, J. W. Waters, and R. S. Harwood (2005), Polar processing and development of the 2004 Antarctic ozone hole: First results from MLS on Aura, *Geophys. Res. Lett.*, *32*, L12817, doi:10.1029/2005GL022582.

Santee, M. L., et al. (2007), Validation of Aura Microwave Limb Sounder $HNO_3$ Measurements, *J. Geophys. Res.*, *112*, D24S40, doi:10.1029/2007JD008721.

Schoeberl, M. R., et al. (2006), Overview of the EOS Aura Mission, *IEEE Trans. Geosci. Remote Sens.*, *44*(5), 1066–1074, doi:10.1109/TGRS.2005.861950.

Solomon, S. (1999), Stratospheric ozone depletion: A review of concepts and history, *Rev. Geophys.*, *37*, 275–316.

Solomon, S., R. R. Garcia, F. S. Rowland, and D. J. Wuebbles (1986), On the depletion of Antarctic ozone, *Nature*, *321*, 755–758, doi:10.1038/321755a0.

Tabazadeh, A., R. P. Turco, K. Drdla, and M. Z. Jacobson (1994), A study of Type I polar stratospheric cloud formation, *Geophys. Res. Lett.*, *21*, 1619–1622, doi:10.1029/94GL01368.

Taylor, F. W., et al. (1993), Remote sensing of atmospheric structure and composition by pressure modulator radiometry from space: the ISAMS experiment on UARS, *J. Geophys. Res.*, *98*, 10,799–10,814, doi:10.1029/92JD03029.

Toon, O. B., P. Hamill, R. P. Turco, and J. Pinto (1986), Condensation of $HNO_3$ and HCl in winter polar stratosphere, *Geophys. Res. Lett.*, *13*, 1284–1287, doi:10.1029/GL013i012p01284.

Urban, J., et al. (2005), Odin/SMR limb observations of stratospheric trace gases: Level 2 processing of ClO, $N_2O$, $HNO_3$, and $O_3$, *J. Geophys. Res.*, *110*, D14307, doi:10.1029/2004JD005741.

Voigt, C., et al. (2000), Nitric acid trihydrate (NAT) in polar stratospheric clouds, *Science*, *290*, 1756–1758, doi:10.1126/science.290.5497.1756.

Walker, K. A., C. E. Randall, C. R. Trepte, C. D. Boone, and P. F. Bernath (2005), Initial validation comparisons for the Atmospheric Chemistry Experiment (ACE-FTS), *Geophys. Res. Lett.*, *32*, L16S04, doi:10.1029/2005GL022388.

Wang, D. Y., et al. (2007), Validation of nitric acid retrieved by the IMK-IAA processor from MIPAS/ENVISAT measurements, *Atmos. Chem. Phys.*, *7*, 721–738.

Waters, J. W., et al. (1999), The UARS and EOS Microwave Limb Sounder (MLS) Experiments, *J. Atmos. Sci.*, *56*, 194–218, doi:10.1175/1520-0469(1999)056<0194:TUAEML>2.0.CO;2.

Waters, J. W., et al. (2006), The Earth Observing System Microwave Limb Sounder (EOS MLS) on the Aura Satellite, *IEEE Trans. Geosci. Remote Sens.*, *44*(5), 1075–1092, doi:10.1109/TGRS.2006.873771.

M. J. Alexander, NorthWest Research Associates, 3380 Mitchell Lane, Boulder, CO 80301, USA.

J. Barnett and C. Hepplewhite, Atmospheric, Oceanic and Planetary Physics Department, Oxford University, Oxford OX1 3PU, UK.

P. F. Bernath, C. D. Boone, and K. A. Walker, Department of Chemistry, University of Waterloo, 200 University Avenue West, Waterloo, Ont. N2L 3G1, Canada.

C. Cavanaugh, M. Coffey, C. Craig, T. Eden, G. Francis, J. Gille, C. Halvorson, J. Hannigan, C. Hartsough, R. Khosravi, D. E. Kinnison, B. Mankin, S. Massie, B. Nardi, D. Packman, and V. Yudin, Atmospheric Chemistry Division, National Center for Atmospheric Research, 3450 Mitchell Lane, Boulder, CO 80301, USA. (dkin@ucar.edu)

V. C. Dean, D. Ellis, C. Krinsky, and C. Randall, University of Colorado at Boulder, Boulder, CO 80309, USA.

D. W. Fahey and P. J. Popp, Chemical Science Division, Earth System Research Laboratory, National Oceanic and Atmospheric Administration, 325 Broadway, Boulder, CO 80305, USA.

V. L. Harvey, Laboratory for Atmospheric and Space Physics, 1234 Innovation Drive, Boulder, CO 80303, USA.

A. Lambert and M. L. Santee, Jet Propulsion Laboratory, 4800 Oak Grove Drive, Pasadena, CA 91109, USA.

T. P. Marcy, 730 North 23rd Street, 300, Milwaukee, WI 53233, USA.